LATVIAN JOURNAL of PHYSICS and TECHNICAL SCIENCES

ISSN 0868 - 8257

5

(Vol. 56)

2019

SATURS

CONTENTS

СОДЕРЖАНИЕ

LATVIAN JOURNAL of PHYSICS and TECHNICAL SCIENCES

LATVIJAS FIZIKAS un TEHNISKO ZINĀTŅU ŽURNĀLS

ЛАТВИЙСКИЙ ФИЗИКО-ТЕХНИЧЕСКИЙ ЖУРНАЛ

Published six times a year since February 1964
Iznāk sešas reizes gadā kopš 1964. gada februāra
Выходит шесть раз в год с февраля 1964 года

5 (Vol. 56) • 2019

RĪGA

INDEKSĒTS (PUBLICĒTS) | INDEXED (PUBLISHED) IN

www.scopus.com
www.sciendo.com
EBSCO (Academic Search Complete, www.epnet.com), INSPEC (www.iee.org.com).
VINITI (www.viniti.ru), Begell House Inc/ (EDC, www.edata-center.com).

Izdevēji: Fizikālās enerģētikas institūts, LU Cietvielu fizikas institūts
Reģistrācijas apliecība Nr. 000700221
Redakcija: Krīvu iela 11, Rīga, LV-1006
Tel. +371 67551732
e-pasts: lvjpts@edi.lv
Interneta adrese: www.fei-web.lv

sciendo

LATVIAN JOURNAL OF PHYSICS
AND TECHNICAL SCIENCES
2019, N 5

DOI: 10.2478/lpts-2019-0026

STUDY OF ELECTRICAL PROPERTIES OF BISTABLE SMECTIC-A LIQUID CRYSTAL DISPLAYS

M. Maltisovs[1,2], D. Pikulins[2]

[1] HansaMatrix Innovation, 1 Ziedleju Str., Marupe, LV-2167, LATVIA
E-mail: matiss.maltisovs @gmail.com
[2] Institute of Radioelectronics, Riga Technical University,
12 Azenes Str., Riga, LV-1048, Latvia
E-mail: dmitrijs.pikulins@rtu.lv

Bistable smectic-A (SmA) liquid crystal display (LCD) is one of the most promising devices for smart glass applications due to long-term bistability, low haze at clear state, low transmittance at scatter state and low power consumption. The need of a good simulation model for an LCD becomes apparent during the design of driving system. Liquid crystal (LC) capacitance is critical in the simulation of LCD pixels and is voltage dependent due to the crystal characteristics. Bistable smectic-A LC capacitance model is introduced in the paper. The study describes the most relevant conclusions obtained from the measurements of electric properties of bistable SmA LCD samples and electric equivalent circuit characterization.

Keywords: *bistable, capacitance model, liquid crystal display, smectic-A*

1. INTRODUCTION

Simple parallel RC circuits usually represent the behaviour of liquid crystal displays (LCD) in a variety of situations. These electric circuits are of great practical interest, since they can be used in countless applications ranging from theoretical studies to simulations of LCD elements [1] molecular director axis parallel the surface of the cell.

Due to the anisotropy of LC material, the liquid crystal capacitance C_{LC} is not constant. It varies from a minimum capacitance when no voltage is applied across the LC cell to a maximum capacitance when the LC cell is fully turned on [2]. Thus, the liquid crystal capacitance C_{LC} is bias and time dependent. This mechanism has been thoroughly analysed by some liquid crystal manufacturers and laboratories. However, the formulation is very dependent on the specific liquid crystal type [2], [3].

One particular feature of SmA liquid crystals is a marked hysteresis in their switching to the extent that dielectric re-orientation (or other disturbances of the smectic structure) does not relax when the electric field is removed, dielectrically re-oriented SmA liquid crystals remain in the driven state until further forces are applied [4]–[6]. This is explained via reference of the nature of the processes, which are used to drive such liquid crystals [7], [8].

Existing studies do not provide detailed information on bistable SmA LC operational, electrical properties. Contrary to a majority of studies that have been conducted using small samples <50x50mm, the present research is based on 300x400mm large bistable SmA LC devices. The main goal of the current research is to determine equivalent electric circuit component parameters to simulate a SmA LCD cell, i.e., to create a simulation model which could help in designing a new driving system for SmA LCDs.

2. EXPERIMENTAL PART

A total of two different experimental series have been performed. For these experiments, bistable SmA LCDs have been manufactured by EuroLCDs Ltd. (see parameters in Table 1 and Table 2). LCDs have 300x400mm outer dimensions and active area equally divided into 8 pixels (one pixel is 95x275mm), which can be switched individually or as a single unit if they are connected in parallel [9], [10]. To maintain a constant cell gap, 15µm plastic ball spacers with density of 10pcs/mm^2 have been used. LCs have been supplied by Dow Corning Corporation [7], [8].

Previous study on operational properties showed that the working voltage of bistable SmA LCDs was 13V/µm, clear (transparent or also known as homeotropic) state frequency was 600Hz and scatter (light scattering or also known as focal conic) state frequency was 30Hz [12].

Table 1

LCD Parameters

Dimensions	300x400mm
Spacer Size	15µm
Liquid Crystal Type	Smectic-A
ITO Resistance	80 Ω/sq

Table 2

LCD Operational Properties

Driving Voltage	13V/µm
Driving Waveform	DC balanced square wave
Scatter Frequency	30Hz
Clear Frequency	600Hz

The LC cell can be considered as an ideal capacitor. Due to its construction, it is very similar to a flat capacitor, where both plates are made up of two indium tin oxide (ITO) layers and between them there is LC material with ε_r [10]. More precisely is to take into account conductivity loss and LC cell approximation in a narrow band with a non-ideal capacitor model (Fig. 3), where R is the electrical

resistance of the output (ITO layer and dielectric) and C is the electrical capacity of a flat capacitor. By adding additional R and C elements, a model describing the LC cell up to a frequency range of 10^{-1}–10^{7}Hz can be obtained [1], molecular director axis parallel the surface of the cell.

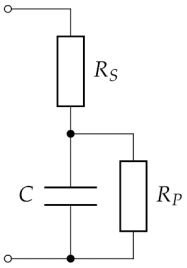

Fig. 1. LC cell equivalent electrical circuit, where R_S – ITO layer and dielectric resistance, C – liquid crystal capacitance and R_p – liquid crystal resistance.

The first experiment has been devoted to obtaining R_S that mainly consists of conducting, transparent layer, ITO resistance measured in ohms per square (Ω/sq). Typical values are 40–100Ω/sq. The thicker ITO layer, the lower resistance and optical transmittance and vice versa. To achieve high optical transmittance and good conductivity, ITO resistance must be chosen between 80–100Ω/sq. Additionally, ITO layer must be patterned to reduce LC breakdown. ITO must be patterned in strips such that the resistance of the strips would increase, thus lowering the current in the series. The great benefit of using patterned electrode is that the overall resistance of the cell does not change, and the capacitive charging times of the cell are not affected. Unfortunately, the patterning is visible to the eye since it scatters light. Compromise between the optical quality and electrical properties should be found [11], [13]. Bistable displays, in which an altering field at different frequencies is used for switching from clear to scattering states and vice versa, require electric fields at around 10 V/μm for operation. When operated at such high voltages an electrical breakdown is very likely to occur in the liquid crystal (LC).

Equivalent series resistance R_S (Eq. 1) can be determined by rapidly applying voltage and measuring the voltage on a series-connected resistor ($R_x = 5 - 10\Omega$ (see Figs. 2 and 3). At the first moment of time C is a short circuit and a voltage divider is formed.

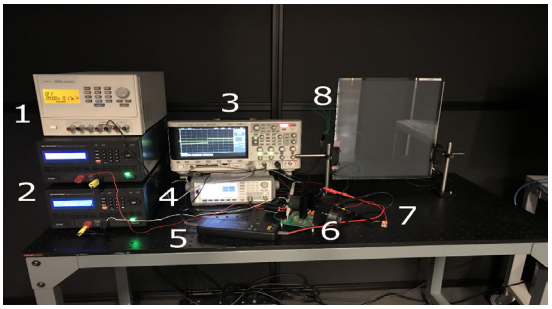

Fig. 2. Overview of the experimental setup used for measuring electrical properties of bistable smectic-A liquid crystal displays. Used equipment: 1 – Agilent U8032A, 2 – B&K Precision 9184, 3 – Agilent DSOX2014A, 4 – Agilent 33500B, 5 – Tektronix P5200, 6 – Apex PA93, 7 – R_x, 8 – bistable smectic-A liquid crystal display.

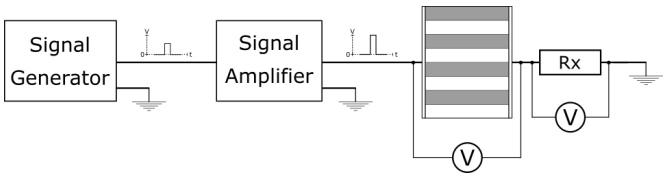

Fig. 3. Simplified functional schematic of electrical parameter measurement setup, where waveform generator generates short 100us square wave impulse, signal amplifier amplifies impulse up to ±190V and outputs signal to bistable smectic-A liquid crystal display and additional resistance.

R_S can be calculated as follows:

$$R_S = \frac{(V_s - V_x)R_x}{V_x}. \tag{1}$$

An effect related to the reorientation experienced by the LC molecules is the change of the capacitance offered by a single LC pixel, C_{LC}. This capacitance depends on the applied voltage because of the dielectric anisotropy of the LC mixture [10].

In the second experiment, the circuit shown in Fig. 4 is used to determine equivalent parallel resistance R_P and capacitance C. In this case V_s is not a rapid voltage step but more gradual and $R_x = 1k\Omega$ (Eq. 2) [14]:

$$\frac{V_x(t)}{R_x} = I_{R_x}(t) = I_C(t) + I_{R_P}(t). \tag{2}$$

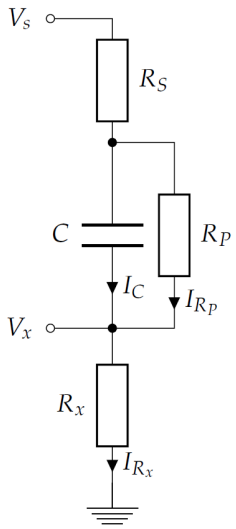

Fig. 4. Electrical schematic of electrical parameter measurement circuit, where V_s – voltage applied to LCD, R_s, R_p and C – liquid crystal display (see Fig. 1 for detailed parameter descriptions), V_x – measured voltage on LCD, R_x – additional resistance.

After certain amount of time C is fully charged, $I_C = 0$ and $I_{R_x} = I_{R_P}$. Since $R_S \ll R_x, R_P$, then R_P can be calculated according to the voltage divider formula (Eq. 1).

When R_P is found I_C can be calculated as follows:

$$I_C(t) = I_{R_x}(t) = I_{R_x}(t) - I_{R_P}(t) = \frac{V_x(t)}{R_x} - \frac{V_s - V_x(t)}{R_P}. \quad (3)$$

Total charge accumulated on the capacitor can be obtained by integrating $I_C(t)$:

$$Q_C = \int I_C(t)dt. \quad (4)$$

Fully charged equivalent capacitor capacity can be calculated as follows:

$$C = \frac{Q_C}{V_s - V_x}. \quad (5)$$

An LC with high viscosity needs high electric field for operation. In large electric fields, electrical breakdown is likely to occur. Electrical breakdown in the cell is observed when the electric field intensity E in the LC layer is above a specific breakdown value E_{br}. The E_{br} is governed by the conductivity of the liquid crystal, surface smoothness of the electrodes, defects in coatings as well as point defects, such as dust particles, in the LC layer. The dielectric breakdown in an LC cell is a complicated process discussed elsewhere [15]. Based on the parameters of the equivalent electrical circuit, it is possible to calculate power dissipation on R_S and R_P:

$$R_P(t) = I_x^2(t) \cdot R_S = R_S \cdot \frac{V_x^2(t)}{R_x^2}. \quad (6)$$

$$P_R(t) = \frac{U_c^2(t)}{Rp} = \frac{(V_s(t) - V_x(t) \cdot (1 + \frac{R_S}{R_x}))^2}{R_P}. \quad (7)$$

3. RESULTS AND DISCUSSION

The results obtained for the measurements of equivalent series resistance R_S are shown in Fig. 5. Two different R_x values were used (5.2Ω, 10.4Ω). The measurements were made at several V_s values ranging from 5V to 195V with 5V increment step. Blue dots represent $R_x = 5.2\Omega$ and orange dots – $R_x = 10.4\Omega$. The green line represents the mean value of both R_x value measurement data. Pronounced deviation is noticeable in 5V to 30V range. When the LC cell is energized, switching is gradually taking place. This is due to the low rotational force caused by the electric field applied to liquid crystal molecules if they are in the lowest energy state. From 40V to 195V R_S does not depend on the applied voltage and $R_S \approx 71\Omega$.

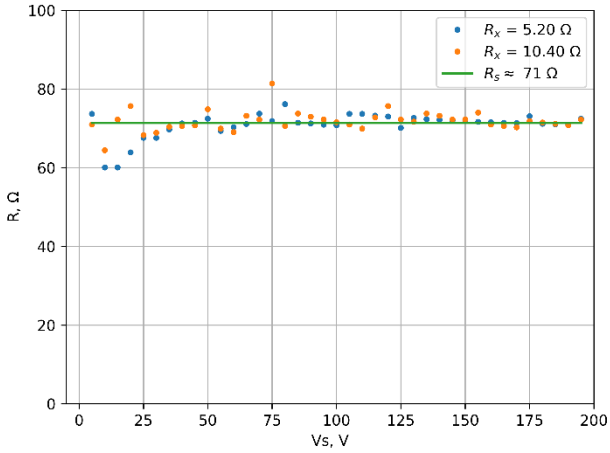

Fig. 5. Equivalent series resistance R_S dependence of V_S, with R_x – 5.2Ω and 10.4Ω over 5V-195V range with 5V increment step. Green line – mean value of both R_x value measurement data, $R_S \approx 71\Omega$.

The results obtained for the measurements of equivalent parallel resistance R_P are shown in Fig. 6. Dotted blue line represents measured R_P and the orange line – the calculated mean value of R_P in LCD working range of 100V–195V. From 5V to 20V, there is an increase in resistance as it should be with different LC materials (for example, cholesteric LC) were R_P increases up to $1M\Omega$. In this case, a rapid decrease follows, and parallel resistance decreases to ≈ 13.5kΩ and from 125V to 195V stays within 5 % deviation. Low resistance is explained by the difference of the liquid crystal composition itself.

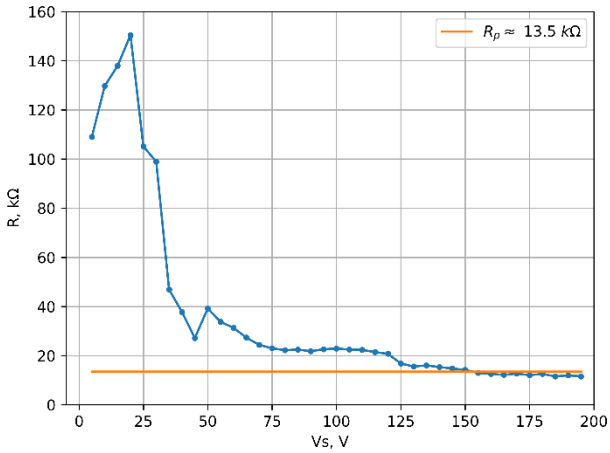

Fig. 6. Equivalent parallel resistance R_P dependence of V_S, with R_x – 1kΩ and over 5V–195V range with 5V increment step. Orange line – mean value of R_P in LCD working range of 100V–195V, $R_p \approx 13.5k\Omega$.

Measured LCD C capacitance changes over 5V to 195V range of V_s (see Fig. 7). Dotted blue line represents C and the orange line – a mean value of C in LCD working range of 100V–195V. Measured capacitance from 5V to 45V $C \approx 0.044\mu F$ with a slight drop at 35V. Then, increasing V_s, the capacitance increases

to 100V and $C \approx 0.053\mu F$. Continuing increasing the voltage capacitance, the value changes within 10 % range. Liquid crystal material dielectric permeability depends on the position of the molecules and can be influenced by the external electric field; C also depends on the applied electric field and it is not linear.

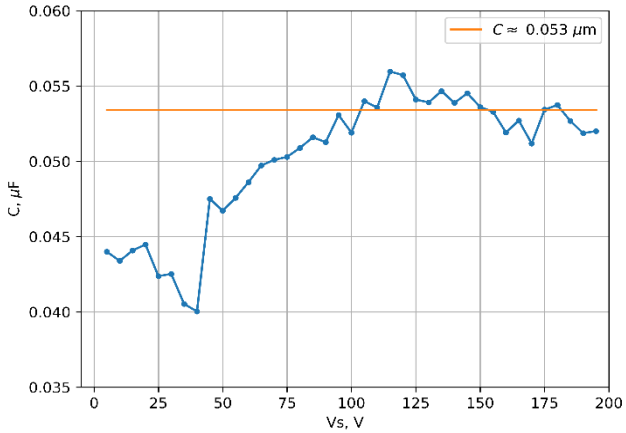

Fig. 7. LCD cell capacitance C dependence of V_S, with R_x – 1kΩ and over 5V–195V range with 5V increment step. Orange line – a mean value of C in LCD working range of 100V–195V, $C \approx 0.053\mu F$.

The obtained power dissipation results on R_S and R_P are shown in Fig. 8. Dotted orange line represents R_P and dotted blue line – R_S resistance. At 195V V_S, which is the typical operational voltage of used LCD samples, $R_S \approx 2.1W$ and $R_P \approx 6.3W$. Both the equivalent parallel and series resistance show exponential growth. Most of the power is dissipated on R_P. R_P can be reduced by minimising voltage; however, this would affect the LCD switching speeds and optical parameters. R_S cannot be reduced due to the proportional current required by the LCD to charge its equivalent capacity.

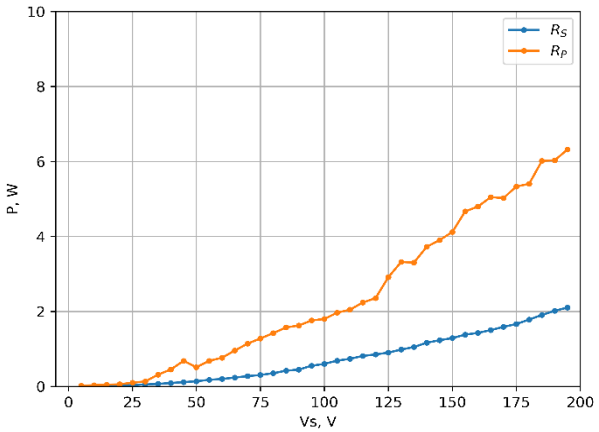

Fig. 8. R_S and R_P power dissipation dependence of V_S, with R_x – 1kΩ and over 5V–195V range with 5V increment step. Dissipated power at LCD operational voltage 195V (see Table 2) – Blue line: $R_S \approx 2.1W$, orange line: $R_P \approx 6.3W$.

4. CONCLUSIONS

1. The experimentally obtained dependence of equivalent series, parallel resistance and bistable smectic-A capacity on applied control voltage has been presented in the paper.
2. The equivalent series R_S and parallel resistance R_P studies show that R_S stays within manufacturers' provided ITO tolerances and do not depend on applied voltage. R_P resistance is much lower compared to other LCD parallel resistance with different LC materials (for example, cholesteric LC).
3. Capacitance C measurements give information about LCDs working range 100V–195V, at which the applied electric field is high enough to be able to rotate LC molecules and change LCD state from transparent to scattering and vice versa. Additional in-depth research should be done in 5V–95V range to fully understand LC molecule threshold voltage at which they start to rotate.
4. Great attention should be paid to power dissipation because with such a low internal parallel resistance LC can quickly reach its temperature limit and LCD will stop working.
5. Simulation model parameters $R_S = 71\Omega$, $R_P = 13k\Omega$, $C = 53nF$ will provide sufficient information about electric functionality of large size 300x400mm bistable smectic-A liquid crystal displays and can be integrated into the development of larger systems.

Further research will be focused on additional experiments with bistable smectic-A liquid crystal displays due to unknown behaviour in long-term functionality, long-term switching tests to understand degradation boundaries for LC and LCD, driving waveform impact on the power consumption and optical parameters, etc.

REFERENCES

1. Aoki, H. (1996). Dynamic characterization of a-Si TFT-LCD pixels. *IEEE Transactions on Electron Devices*, *43*(1), 31–39. https://doi.org/10.1109/16.477590
2. Bahadur, B. (1990). *Liquid crystals — applications and uses* (vol. 1). Canada: Litton Systems Canada. https://doi.org/https://doi.org/10.1142/1013
3. Choi, T.-H., Do, S.-M., Jeon, B.-G., & Yoon, T.-H. (2019). Low-power control of haze using a liquid-crystal phase-grating device with two-dimensional polymer walls. *Optics Express*, *27*(3), 3014. https://doi.org/10.1364/oe.27.003014
4. Clapp, T. V., Crossland, W. A., Davey, A. B., Grassman, M., Hannington, J. P., King, R. K., … Xu, H. (2011). *Liquid crystal formulations and structures for smectic a optical devices*. Retrieved from http://www.dowcorning.com/content/paintink/paintinkresin/default.aspx
5. Costa, M. R., Altafim, R. A. C., & Mammana, A. P. (2006). Electrical modeling of liquid crystal displays-LCDs. *IEEE Transactions on Dielectrics and Electrical Insulation*, *13*(1), 204–209. https://doi.org/10.1109/TDEI.2006.1593418
6. Cristaldi, D. J. R., Pennisi, S., & Pulvirenti, F. (2009). *Liquid Crystal Display Drivers: Techniques and Circuits*. Springer Netherlands. https://doi.org/10.1007/978-90-481-2255-4

7. Gotlaufs, R. (2018). *Electrically Controllable Optical Diffusers and Development of an Improved Electrical Drive Circuit.* Riga: Riga Technical University.
8. Hannington, J. P., Clapp, T. V., Nishida, F., King, R. K., Farooq, O., Grassman, M., … Pivnenko, M. (2013). *Oligosiloxane modified liquid crystal formulations and devices using same (US Patent)*.
9. Huh, J. W., Ji, S. M., Heo, J., Yu, B. H., & Yoon, T. H. (2016). Bistable light shutter using dye-doped cholesteric liquid crystals driven with crossed patterned electrodes. *Journal of Display Technology*, *12*(8), 779–783. https://doi.org/10.1109/JDT.2016.2537827
10. Karmakar, G., Roy, S., Chattopadhyay, G., & Xiao, Z. (2017). Dynamically controlling exterior and interior window coverings through IoT for environmental friendly smart homes. *Proceedings – 2017 IEEE International Conference on Mechatronics, ICM 2017*, 487–491. https://doi.org/10.1109/ICMECH.2017.7921156
11. Lan, Z., Li, Y., Dai, H., & Luo, D. (2017). Bistable smart window based on ionic liquid doped cholesteric liquid crystal. *IEEE Photonics Journal*, *9*(1). https://doi.org/10.1109/JPHOT.2017.2653862
12. Lueder, E. (2010). *Liquid crystal displays: Addressing schemes and electro-optical effects* (2nd ed.). Wiley. Retrieved from https://www.wiley.com/en-lv/Liquid+Crystal+Displays%3A+Addressing+Schemes+and+Electro+Optical+Effects%2C+2nd+Edition-p-9780470688182
13. Maltisovs, M., Krumins, K., Ozols, A., & Pikulins, D. (2018). Study of the operational properties of bistable smectic-a liquid crystal displays. *Latvian Journal of Physics and Technical Sciences*, *55*(3), 54–62. https://doi.org/10.2478/lpts-2018-0021
14. Mozolevskis, G., Ozols, A., Nitiss, E., Linina, E., Tokmakov, A., & Rutkis, M. (2015). Reduction of electric breakdown voltage in LC switching shutters. *Latvian Journal of Physics and Technical Sciences*, *52*(5), 47–57. https://doi.org/10.1515/lpts-2015-0028
15. Neusel, C., & Schneider, G. A. (2014). Size-dependence of the dielectric breakdown strength from nano- to millimeter scale. *Journal of Mechanics and Physics of Solids, 63,* 201–213. https://doi.org/10.1016/j.jmps.2013.09.009

BISTABILO SMECTIC-A ŠĶIDRO KRISTĀLU DISPLEJU ELEKTRISKO PARAMETRU IZPĒTE

M. Maltisovs, D. Pikuļins

K o p s a v i l k u m s

Bistabilie Smectic-A (SmA) LCD ir viena no daudzsološākajām tehnoloģijām gudro stiklu produktu izstrādei, pateicoties ilgstošai bistabilitātei, augstai gaismas caurlaidībai caurspīdīgā stāvoklī, zemai gaismas caurlaidībai gaismu izkliedējošā stāvoklī un zemajiem energoresursu patēriņiem. Vajadzība pēc laba šķidrā kristāla simulācijas modeļa parādās vadības sistēmas izstrādes laikā. Šķidro kristālu (LC) kapacitāte ir kritiska LCD pikseļu simulēšanā un ir atkarīga no sprieguma šķidrā kristāla īpašību dēļ. Pētījuma ietvaros tika veikti šķidro kristālu displeju virknes, paralēlo pretestību, kapacitātes un jaudas mērījumi. Izdarīti secinājumi par iegūtajiem rezultātiem, izteikti priekšlikumi turpmākajiem pētījumiem.

17.10.2019.

sciendo

LATVIAN JOURNAL OF PHYSICS
AND TECHNICAL SCIENCES
2019, N 5

DOI: 10.2478/lpts-2019-0027

NOISE IMMUNITY OF THE FIBONACCI COUNTER WITH THE FRACTAL DECODER DEVICE FOR TELECOMMUNICATION SYSTEMS

S. Matsenko[1, 2], O. Borysenko[1], S. Spolitis[2], V. Bobrovs[2]

[1]Department of Electronics and Computer Technology, Sumy State University,
2 Rymskogo-Korsakova Str., Sumy, 40007, UKRAINE
[2]Institute of Telecommunications, Riga Technical University
12 Azenes Str., Riga, LV-1048, LATVIA
Svitlana.Matsenko@rtu.lv

The paper presents the improved method of noise immune Fibonacci counting in the minimal form of representation. The method was tested and investigated in the developed noise immune pulse counter based on a minimal form of Fibonacci code with a fractal decoding device. The proposed device, which is simulated in the NI Multisim software, possesses a homogenous structure, increased noise immunity, performance and detection of bit errors in the process of its operation.

Keywords: *Fibonacci code, fractal decoding device, minimal form, noise immunity, pulse counter, telecommunication systems.*

1. INTRODUCTION

Digital devices are determined by the structural characteristics of components of these devices, the improvement of which remains topical in our time. These devices can be implemented based on noise immunity number systems, among which the Fibonacci number system is distinguished [1]–[14].

The advantage of using noise immune number systems in digital devices is that the introduction of natural redundancy takes place at the stage of choosing the form of information representation. This allows for end-to-end control over the transmission and processing of information in digital devices. In addition, the use of noise immune number systems allows, in some cases, synthesising digital devices and components more noise immune and high-speed than using conventional binary number systems [6]–[9]. The feature of digital devices operating by noise immune number systems is that the redundancy necessary for detecting errors is evenly distributed in the structures of the digital scheme. Additional control schemes in them are either not used at all or are used with minimal hardware costs [10]–[14].

Decoders and pulse counters are the components of digital devices. The

counters, without decoding, synthesised based on the noise immunity number systems have high noise immunity but do not have the ability of decoding, which is necessary for their practical application.

Today, interest in Fibonacci codes is growing, as evidenced by a number of publications [1], [2], [10]–[14]. In this paper, we used the Fibonacci code in the minimal form of representation to build a high-speed noise immune counter with the fractal decoder device. This allows corresponding digital devices to be noise immune in other forms of the Fibonacci code representation. The noise immunity of pulse counter based on the minimal form of the Fibonacci code with a fractal decoding device can be used in high-speed telecommunication systems for collection and transmission of information. The use of Fibonacci codes in the telecommunication systems for collecting and transmitting information significantly increases the noise immunity and speed of information transfer. The device in the form of the Fibonacci counter with decoding also refers to automation and computing devices and can be used in systems of discrete information processing as a noise immune counter, pulse distributor, and the noise immune information coding device. The goal of the research is achieved through the introduction of new design features that provide efficient decoding of the counter states.

2. THE FIBONACCI CODE IN THE MINIMAL FORM OF REPRESENTATION

The Fibonacci numbers are the following sequence: 0, 1, 1, 2, 3, 5, 8, 13… F_n. Each number in it, starting with the third, is defined as the sum of the two previous elements: $F_n = F_{n-1} + F_{n-2}$, $F_1 = F_2 = 1$. In this paper, investigation of the Fibonacci code in a minimal form of representation is performed. Fibonacci code in the minimal form of representation by the following numerical function: $N = a_n F_n + a_{n-1} F_{n-1} + ... + a_i F_i + ... + a_1 F_1$, where $a_i \in \{01\}$ is the binary digit of the *i*-th bit of the positional representation of the number; *n* is the code length; F_i is the weight of the *i*-th bit, which equals the *i*-th Fibonacci number [4]. The appearance of such combinations indicates the presence of errors. Table 1 shows, for example, the Fibonacci code for *n* = 5, where *n* – the code length.

Table 1

The Fibonacci Code for the Code Length *n*=5

No.	The Fibonacci code					No.	The Fibonacci code				
	8	**5**	**3**	**2**	**1**		**8**	**5**	**3**	**2**	**1**
0	0	**0**	**0**	**0**	**0**	**8**	1	**0**	**0**	**0**	**0**
1	0	**0**	**0**	**0**	**1**	**9**	1	**0**	**0**	**0**	**1**
2	0	**0**	**0**	**1**	**0**	**10**	1	**0**	**0**	**1**	**0**
3	0	**0**	**1**	**0**	**0**	**11**	1	**0**	**1**	**0**	**0**
4	0	**0**	**1**	**0**	**1**	**12**	1	**0**	**1**	**0**	**1**
5	0	1	0	0	0						
6	0	1	0	0	1						
7	0	1	0	1	0						

The characteristic feature of the Fibonacci code in the minimal form of representation is that it does not contain two consecutive units. Thus, the code combination 11 is forbidden for the Fibonacci code in the minimal form of representation [4].

3. THE METHOD OF NOISE IMMUNITY OF THE FIBONACCI COUNTING

Based on the Fibonacci number system, the method of counting possesses increased high speed, noise immunity and simplicity [1]. The advantage of the method is the absence of operations of the Fibonacci number transition from the minimal form to the maximal form and back, as is the case in the number of existing methods for counting Fibonacci numbers, which increases counting speed [1], [2].

The working principle of the noise immune Fibonacci counter is based on finding two bits with two 0 in the Fibonacci number, when counting from right to left, and then setting the first bit to 1, while converting the low-order bits to zero [5], [14]. For example, if the Fibonacci number 01001000 in the minimal form is 26, then, in accordance with the proposed method, the next number equal to 01001001 is 27.

The method of the noise immune counting of Fibonacci numbers consists of the following sequential steps:

1. The counting begins with code combinations containing zeros.
2. The lower-order bit of the code combination containing 0 is converted to 1.
3. Then 1 is converted to 0, and 1 is put in front of 0.
4. The lower-order bit of those containing two consecutive zeros, with the counting from right to left, 0 converted to 1. The lower-order bits, standing to the right of 1, are converted to 0.
5. If there is one zero in front of the high-order bit unit of the code combination, and there are not two zeros standing next to each other, then the zero before the high-order unit is converted to 1. All other low-order bits convert to 0.
6. The counting goes until the Fibonacci code combination appears, in which between units there is only one zero, and in front of the high-order bit 1, there is not more than one zero.
7. The appearance of two consecutive units in the Fibonacci code combination is a sign of an error.

For example, the 5-digit counting using the above method is shown in Table 1. The counting in this case begins with the initial code combination 00000, consisting of bits containing zeros. Then, the low-order bit is converted to 1. As a result, the combination 00001 is obtained. Since only zeros are in front of this 1, it is converted to 0 in the next step of the method, and 1 is put in front of the resulting 0, which results in the code combination 00010. In front of 1 there are only zeros, it follows that in the next step of the method 1 is converted to 0, and 0 in front is converted to 1, which results in the code combination 00100. Since in the lower bits – zero, then in

the next step of the method 1 is converted to 0, which results in the code combination 00101.

The presence of one zero between the zero bit and second bit results in the next 1 entered to the fourth bit. In this case, all bits to the right of the third bit reset to 0, which results in the code combination 01000. Then the counting process continues until there is one zero between the units in the Fibonacci number, and zero or one in the most significant bit is 10101.

The method allows applying the simple and effective algorithm of detecting errors such as transitions 0 to 1, since the method is based on the sign of the absence of two or more adjacent 1. Based on this method, the noise immune, high-speed Fibonacci counter is implemented [14]. Figure 1 shows the method of noise immune counting of Fibonacci numbers.

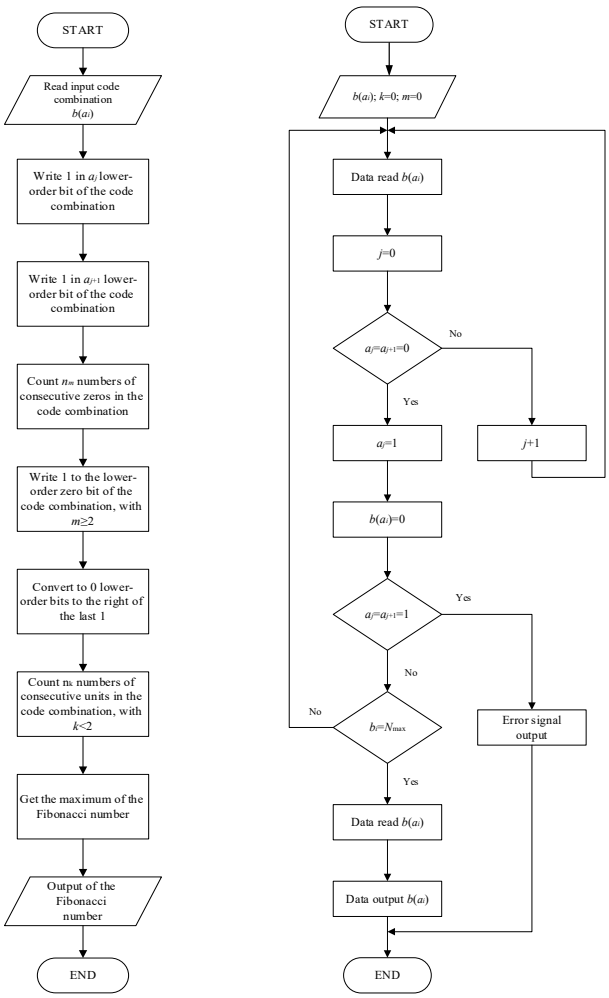

Fig. 1. (a) General block diagram of noise immune counting of Fibonacci numbers;
(b) Block scheme of noise immune counting of Fibonacci numbers, where $b(a_j) = a_j \ldots a_0$ – Fibonacci code sequence; m – a number of zeros in the code combination;
k – a number of units in the code combination; N_{max} – maximal of the Fibonacci number.

4. EVALUATION OF NOISE IMMUNITY OF THE FIBONACCI CODE

The share of errors detected by the noise immune code is determined by the equation (1) [1]:

$$D = 1 - \frac{M}{N}, \qquad (1)$$

where M is the number of allowed code combinations; N is the number of all code combinations equal to 2^n.

Table 2 shows the share of detected errors D of the Fibonacci code for n = 10, 15, 20, 25, 30, 40, where the n is code length.

Table 2

The Share of Detected Errors *D* of the Fibonacci Code

n	*D*	*n*	*D*
10	0.859	25	0.994
15	0.951	30	0.998
20	0.983	40	0.999

The share of the detected errors of the Fibonacci code from the code length n is shown in Fig. 2.

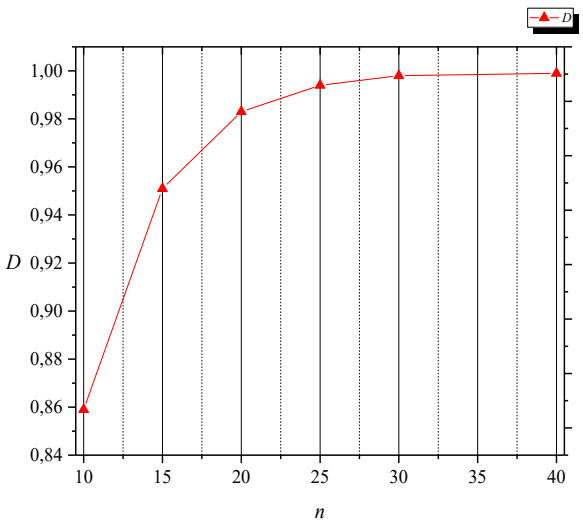

Fig. 2. The share of the detected errors by the Fibonacci code if different code lengths n are used.

From Fig. 2 it follows that the share of the detected errors by the Fibonacci code with increasing n tends to 1.

5. DEVELOPMENT OF HIGH-SPEED NOISE IMMUNE COUNTER WITH FRACTAL DECODING DEVICE

The functional diagram of the high-speed counter based on the minimal form of the Fibonacci code with the fractal decoder device for $n = 5$ is shown in Fig. 3. The Fibonacci fractal decoder device consists of switching device 1, containing $2n$ elements AND 1.1 - AND 1.10, a decoding block 2 consisting of elements NOT 2.1, OR 2.1, NOR 2.2, OR 2.3. The structure of the fractal decoder consists of linear decoders: Decoder 1 (DC1) and Decoder 2 (DC2). The linear decoder DC1 consists of n-1 inputs and n outputs. The linear decoder DC2 consists of n inputs and n-2 outputs. The structure of high-speed noise immune pulse counter consists of control unit 3, containing the element OR 3.1 and elements AND 3.1 - AND 3.4. The disposition unit 4 consists of elements AND 4.1 - AND 4.4 with inverters at the inputs. The analysis unit 5 consists of elements AND 5.1 - AND 5.4. The register 6 contains flip-flops TT 6.1 - TT 6.5 and elements AND 6.1 - AND 6.5. The counter zero-setting unit 7 consists of the elements OR 7.1 - OR 7.4. The high-speed pulse counter based on Fibonacci codes works as follows. In the initial position, flip-flop of register 6 is set to zero. The first clock pulse sets the first flip-flop TT 6.1 to 1 and prohibits the passage of signal to the flip-flops TT 6.2 - TT 6.5.

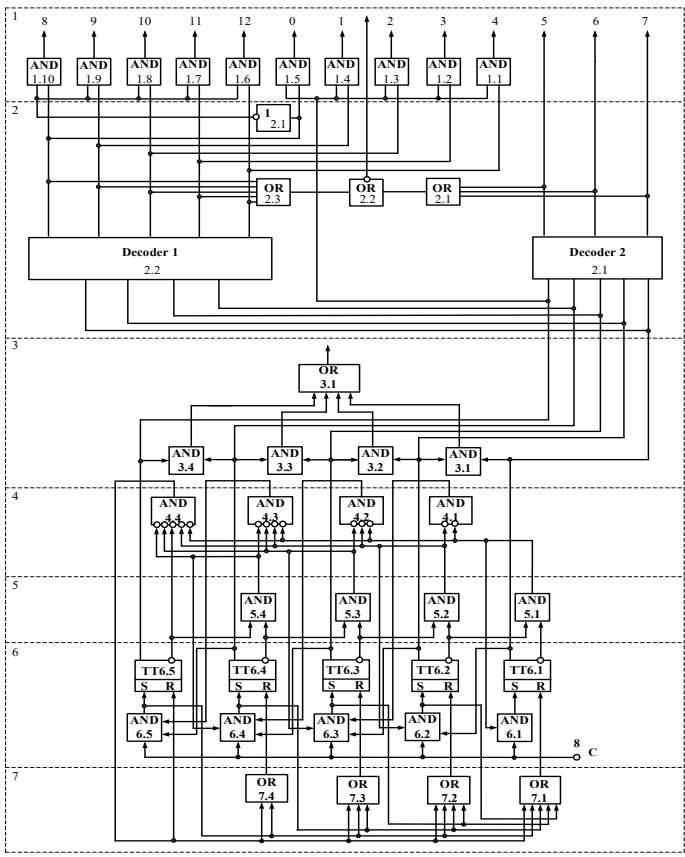

Fig. 3. Functional diagram of the high-speed noise immune counter with the fractal decoder device.

The second clock pulse sets the first flip-flop TT 6.2 to 1 by the enabling signal from the direct output of the first flip-flop TT 6.1. The flip-flop TT 6.1 is set to 0 by the counter zero-setting unit 7.

The third clock pulse sets to 1 the third flip-flop TT 6.3, since the enabling signals are supplied from the disposition unit 4, the analysis unit 5 and the second flip-flop TT 6.2. The first and second flip-flops TT 6.1 - TT 6.2 are set to zero by the counter zero-setting unit 7.

The fourth clock pulse sets the flip-flop TT 6.1 to 1, while the flip-flop TT 6.3 is also in 1 by signal from the disposition unit 4. This procedure is repeated until the code combination is obtained, in which there is one zero between two units [14]. The high-speed Fibonacci counter operates in accordance with Table 1.

In the initial position, all flip-flops of register 6 are set to zero, which corresponds to code combination 00000. The first clock pulse sets the flip-flop TT 6.1 to 1, through the first input of the element AND 6.1, to which the signal arrives from the bus 8. The signal 1 from the output of the element AND 5.1 of the analysis unit 5 arrives at the second input of the element AND 6.1, thus the following code combination 00001 is obtained.

The flip-flops TT 6.2 - TT 6.5 are set to zero, since zero signals from the outputs of other elements arrive at the inputs of the elements AND 6.2 - AND 6.5. The presence of 1 in the low-order bit and zeros in the remaining bits gives the possibility of recording 1 to the second bit.

The second clock pulse sets the flip-flop TT 6.2 to 1. The signal 1 from the direct output of the flip-flop TT 6.1 arrives at the first input of the element AND 6.2. The signal 1 from the output of the element AND 5.2 of the analysis unit 5 arrives at the third input of the element AND 6.2. Two ones from the inverse outputs of the flip-flops TT 6.1, TT 6.3 of the register 6 arrive at the inputs of the element AND 5.2. Zero signals from the elements AND 6.3 - AND 6.5 of the register 6 and the element AND 4.4 of the disposition unit arrive at the inputs of the OR 7.1 element, since the flip-flops TT 6.3 - TT 6.5 are set to zero. As a result, the single signal appears at the direct output of the flip-flop TT 6.2. Thus, the code combination 00010 is obtained.

The third clock pulse sets the flip-flop TT 6.3 to 1. The signal from the direct output of the flip-flop TT 6.2 arrives at the second input of the element AND 6.3. The signal from the output of the element AND 5.3 of the analysis unit arrives at the fourth input of the element AND 6.3, since 1 arrives at the input AND 5.3 from the inverse outputs of the flip-flops TT 6.3 and TT 6.4. The signal 1 from the output of the element AND 4.1 of the disposition unit 4 arrives at the first input of the element AND 6.3, since the zero signal arrives at the first input AND 6.2, which is the output of the direct flip-flop TT 6.1. As a result of the inverse outputs of the flip-flops TT 6.1 and TT 6.2, the zero signal arrives at the element AND 5.1 of the analysis unit 5. From the output of the element AND 5.1, the signal arrives at the elements NOT, after the signal arrives at the element AND 4.1. At the same time, from the output of the element AND 6.3, the signal 1 arrives at the first input of the element OR 7.2 and from its output at the second input of the element OR 7.1 of the counter zero-setting unit 7, the output of which is connected to the reset input of flip-flop TT 6.1. Thus, the flip-flops TT 6.1 and TT 6.2 are set to zero. Thus, the code combination 00100 is obtained [14].

The fourth clock pulse sets the flip-flops TT 6.1 and TT 6.3 of the register 6 to 1. The signal 1 from the bus 8 arrives at the first input of the element AND 6.1. The signal 1 from the output of the element AND 5.1 of the analysis unit 5 arrives at the second input of the element AND 6.1. Thus, the flip-flop TT 6.1 is set to 1. The signal 1 from the inverse output of the flip-flop TT 6.1 arrives at the first input of the element AND 5.1 of the analysis unit 5.

Zero arrives at the second input of the element AND 5.1 from the inverse output of the flip-flop TT 6.2. The signal 0 from the TT 6.1 arrives at the first input of the element AND 5.1. The signal 0 from the output of the element AND 5.1 arrives at the first input of the element NOT of the disposition unit 4.

Zero arrives at the second input of the element NOT of the disposition unit 4 from the output of the element AND 5.2, after which the signal arrives at the element AND 4.1 from the output of the element AND 4.1. The signal of 1 arrives at the first input of the element AND 6.3, as the input elements AND 4.1 are inverters. The flip-flop TT 6.2 is set to 0 by the signal from the output of the element AND 5.2. Thus, the code combination 00101 is obtained. The logic waveforms of the operation of each of the incoming blocks in the device are shown in Fig. 4.

The counting continues until the maximum of the Fibonacci number 10101 is obtained. After the appearance of the maximum Fibonacci number, the counting ends, the register is set to 0, after which a new counting cycle begins [14].

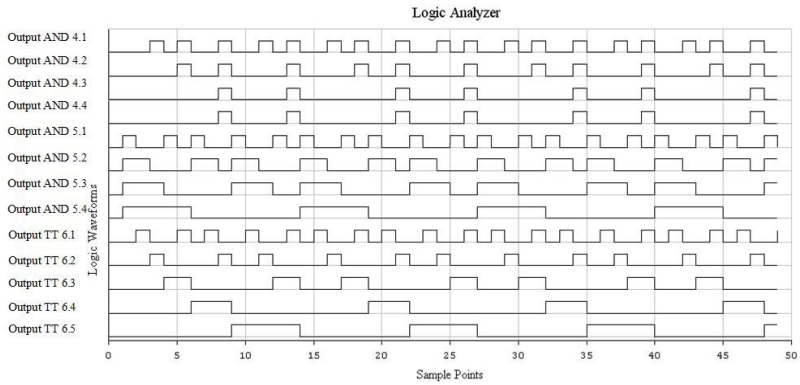

Fig. 4. The logic waveforms of the high-speed counter based on the minimal form of the Fibonacci code.

The device contains the 2-input elements AND 3.1 - AND 3.4 of the control unit 3 for analysing the correct operation of the counter, the outputs of which are connected by the 4-input element OR 3.1, and the inputs are connected to the direct outputs of two adjacent flip-flops. If an error occurs as a result of counting, which is characterised by the appearance of two adjacent units in the Fibonacci bits, then signal 1 appears at one of the elements AND 3.1 - AND 3.4 and an error signal appears at the output of the element OR 3.1 [14].

The presence of parallel chains of transfer signals in the disposition unit 4 and the counter zero-setting unit 7 significantly increases the speed of the Fibonacci counter, and the use of the code Fibonacci based on the device determines its advantage over binary counters by the noise immunity criterion.

The decoding using the fractal decoder device is as follows: 4 low-order bits of the first five Fibonacci bits are repeated in five numbers at the end of Table 1. The difference between these groups of bits is the presence of zero or one in the high-order bit, which characterises fractal structure of Fibonacci code [15].

At the initial position, one of the code combinations shown in Table 1 goes to the inputs of the first and second decoder DC 2.1, DC 2.2. The first decoder DC 2.1 decodes the code combinations corresponding to the numbers 0–4 and 8–12 in Table 1, the second decoder DC 2.2 decodes the code combinations corresponding to the numbers 5–7 in Table 1. When the combination of 0–4 or 8–12 arrives at the DC1, signal 1 appears at one of the elements AND 1.1–AND 1.10 of switching device 1.

If the counter is in state 00001, which corresponds to signal 1 at the output of the element AND 1.4 of switching device 1, all other outputs of switching device 1 are set to 0, which is the result of decoding. Other code combinations are decoded by the usual method [15]. If, as a result of decoding, an error occurs, which is characterised by the appearance of two units that are next to each other in the Fibonacci bits, then signal 1 arrives at the element OR 2.2, which indicates the presence of errors. The operation of noise immune high-speed Fibonacci counter with the fractal decoder device is simulated in the NI Multisim simulation and analysis system.

6. CONCLUSIONS

In this paper, the method of noise immunity of the Fibonacci counting in the minimal form of presentation has been improved. The authors of the paper have also developed the noise immune pulse counter with fractal decoding based on the minimal form of the Fibonacci code. This device possesses a homogeneous structure, as well as increased noise immunity due to the detection of bit errors in the operation. The operation of the noise immune high-speed Fibonacci counter with the fractal decoder device has been simulated in the NI Multisim software. The proposed noise immune pulse counter can be used in high-speed telecommunication systems for the transmission of information in very noisy channels. The use of Fibonacci codes in telecommunication systems for collecting and transmitting information significantly increases the noise immunity and speed of information transfer. The device such as the Fibonacci counter with decoding also refers to automation and computing devices and can be used in systems of discrete information processing as a noise immune counter, pulse distributor and noise immune information coding device. The goal of the research is achieved through the introduction of new design features that provide the decoding of the counter. The research will be continued in the future with the implementation of the Fibonacci counter using the fractal decoder device in the field-programmable gate array.

REFERENCES

1. Stakhov, A. (2017). *Numeral systems with irrational bases for mission-critical applications*. Singapore; New Jersey: World Scientific Publishing Co. Pte. Ltd.
2. Stakhov, A. (2012). *Fibonacci* and *golden proportion codes* as an *alternative* to the *binary numeral system.* Germany: Academic Publishing.

3. Hoggatt, V. E. (1969). *Fibonacci and Lucas numbers*. Boston: Houghton Mifflin.
4. Vorobyov, N. (1978). *Fibonacci numbers.* Moscow: Nauka.
5. Stakhov, A., Borisenko, A., & Matsenko, S. (2014). Fibonacci Counter based on Zeckendorf's Theorem (Boolean Realization). *Visual Mathematics*, *16*(2), 19.
6. United States Patent No. US8983023 B2. (2015). *Digital Self-Gated Binary Counter*, Gupta, N., Agarval A., Goyal, G., No. US 13/935,552; declared: 04.07.2013; published: 17.03.2015.
7. Yeh, C.-H. (2000). *Designs of counters with near minimal counting / sampling period and hardware complexity*. Pacific Grove, CA, USA.
8. Thamaraiselvan, K. A. (2013). High Speed CMOS Parallel Counter Using Pipeline Partitioning. *International Journal of Engineering Research*, *2*(8), 491–495.
9. Bindu, S. A. (2015). Review on High Speed CMOS Counter Using Altera MAX300A. *International Journal of Advanced Research in Computer and Communication Engineering*, *4*(12), 589–592.
10. Borysenko, O., Kalashnikov, V., Kalashnikova, N., & Matsenko, S. (2017). The Fibonacci Numeral System for Computer Vision, Computer Vision in Control Systems-3: Aerial and Satellite Image Processing. *Springer International Publishing AG*, 321–343.
11. Azarov, O. (2015). The high-speed reversible Fibonacci counter. *Information Technology and Computer Engineering*, *1*, 27–32.
12. Azarov, O. (2015). Method of quick decrement count with linear hardware increasing when orders are adding. *Bulletin of the Vinnytsia Polytechnic Institute*, *2*(119), 57–61.
13. Azarov, O. (2014). Method of building the high-speed Fibonacci counters. *Information and management problems*, *2*(46), 5–8.
14. Useful Model Patent No. 89153U, MPK 14 N03K 23/00. (2014). *Pulse counter*, Borysenko, O., Matsenko S., applicant and patentholder Sumy State University, No. u201313302, declared: 15.11.2013, published: 10.04.2014.

FIBONAČI SKAITĪTĀJA TROKŠŅNOTURĪBA AR FRAKTĀLU DEKODĒTĀJA IERĪCI TELEKOMUNIKĀCIJU SISTĒMĀM

S. Matsenko, O. Borisenko, S. Spolītis, V. Bobrovs

K o p s a v i l k u m s

Pētījumā parādīta uzlabota metode, kas domāta trokšņnoturīgai Fibonači skaitīšanai minimālā reprezentācijas formā. Metode tika testēta un izpētīta izveidotajā trokšņnoturīgā impulsu skaitītājā, kurā pamatā ir minimālas formas Fibonači kods ar fraktālu dekodētāja ierīci. Piedāvātajai ierīcei, kas ir simulēta NI Multisim programmatūrā, piemīt homogēna struktūra, paaugstināta trokšņnoturība, veiktspēja, kā arī bitu kļūdu uztveršana darbības procesā.

02.09.2019.

sciendo

LATVIAN JOURNAL OF PHYSICS
AND TECHNICAL SCIENCES
2019, N 5

DOI: 10.2478/lpts-2019-0028

DEVELOPMENT OF INFORMATION MODELS FOR INCREASING THE EVALUATION EFFICIENCY OF WIRELESS CHANNEL PARAMETERS OF 802.11 STANDARD

D. M. Mykhalevskiy*, V. M. Kychak

Department of Telecommunication Systems and Television
Vinnytsia National Technical University,
21021, 95 Khmelnytske Highway, Vinnytsia, UKRAINE
*adotq@ukr.net

The objective of the research is to develop information models in order to improve the efficiency of evaluating the parameters of the wireless channels in 802.11 standard. A feature of the information model of the wireless channel of 802.11 standard is an opportunity to evaluate the efficiency of transferring the information block taking into account the complete packet and frame transmission cycle in the event of errors in frames. In addition, the model accounts for the existence of other subscribers in the network and the mechanism of competition for the physical resource of the frequency channel. It has been established that channel efficiency is mostly affected by the presence of destabilizing factors in the channel, which lead to an increase in the number of service information and an increase in the transmission cycle due to the creation of reciprocal queries.

Keywords: *bandwidth, channel level, effective data rate, physical level, 802.11 standard, wireless channel*

1. INTRODUCTION

One of the common channel building technologies is the 802.11 standard, which includes the function to quickly deploy local area networks in the corporate and home sectors, easy connection of user equipment, and low cost of hardware [1]. The development of the 802.11 standard made a contribution to the widespread introduction of the concept of the Internet of Things and increasing requirements for bandwidth channels.

However, the rapid spread of 802.11 wireless technologies and the emergence of a large number of networks lead to the emergence of a large number of negative factors that can significantly hinder the transmission characteristics of wireless transmission channels [2]. They cause the delays in the channel and errors in accepted packages. This results in an increase in the amount of service information and, as

a result, in a significant impairment in the bandwidth of the channel. It becomes unacceptable for high-quality telecommunication and information communication services. These factors need to be taken into account at the design stages of wireless networks. The most reliable estimation of such factors can be obtained only by applying methods for evaluating network parameters and wireless channels developed on the basis of experimental research. On the other hand, for the exchange of information at the application level there is a mechanism for transmission by the channel, which has its own factors to consider. Therefore, in addition to the experimental methods, it is necessary to have models for assessing the transmission of information in the channel, taking into account the parameters of the relevant transmission mechanism.

Analysing the works [3]–[10], one can say that, as a rule, all existing studies were aimed at obtaining a general information model of a wireless channel and determining the software conditions for maximum productivity. However, the actual rate of transmission has a direct dependence on the destabilizing factors in the channel.

2. GENERAL DEVELOPMENT OF INFORMATION MODEL OF THE WIRELESS CHANNEL

The general information model can be constructed using the following expression [10]–[12]. The efficiency ratio of information transmission in the channel can be written as follows:

$$K_{ef} = \frac{V_{ef}}{V_{pl}}, \tag{1}$$

where V_{ef} – the effective rate of information transmission; V_{pl} – the maximum bandwidth of a channel, which is determined by the rate of frame transformation into a bit sequence at the physical layer.

Let us consider options in terms of information transfer. The effective rate of transmission is an amount of information υ, which is transmitted in the channel for a certain time interval t (2). At the channel layer, depending on the transmission system standard, the information is divided into frames (3), where N_f – the number of frames; L_f – the length of the frame.

$$V_{ef} = \frac{\upsilon}{t}; \tag{2}$$

$$\upsilon = N_f L_f . \tag{3}$$

The time for the transmission of information in the channel is determined based on the frame transfer cycle. The transfer time of frames taking into account errors can be calculated using the expression:

$$t = \left(t_f + t_s\right)\left(N_f + N_e\right), \tag{4}$$

where t_f – frame transmission time; t_s – time of transfer of service information taking into account the frame transmission cycle; N_e – the number of received frames with errors, for which the overwrite procedure is executed.

False frames increase the amount of repeated information transmitted on the channel. They can be expressed via the probability of bit error occurrence. Then the time of the information transfer in the channel can be written as (5), where P is the probability of receiving the error frame:

$$t = N_f\left(t_f + t_s\right)(1 + P). \tag{5}$$

In semi-duplex systems, the transfer of a package is carried out in two stages: a request for the transfer of a package in direct T_x channel and reception confirmation in reverse R_x. Thus, taking into account [4], the delay time for one frame transfer frame can be defined as follows:

$$t_s = t_{Tx} + t_{Rx} = \frac{L_{Tx} + L_{Rx}}{V_{pl}} + 2\,t_{dc}, \tag{6}$$

where t_{Tx} – transmission time of the transfer request frame; t_{Rx} – time to receive a frame confirming the successful transmission of the information frame; L_{Tx} and L_{Rx} – the lengths of the request and confirmation frames, respectively; t_{dc} – the time delay between the frames of the transmission cycle, which is determined by the technical features of the standard.

Considering the transmission cycle of the information frame and the delay in the channel, the effective rate of transmission of information can be calculated by substituting (6), (4) and (3) into (2):

$$V_{ef} = \frac{N_f\,L_f}{\left(t_f + \frac{L_{Tx} + L_{Rx}}{V_{pl}} + 2t_{dc}\right)(Nf + Ne)} = \frac{L_f}{\left(t_f + \frac{L_{Tx} + L_{Rx}}{V_{pl}} + 2t_{dc}\right)(1 + P)}. \tag{7}$$

Taking into account (7), the efficiency ratio of the channel can be calculated as follows:

$$K_{ef} = \frac{L_f}{(1 + P)(\left(t_f\ +\ 2t_s\right)V_{pl}\ +\ L_{Tx}\ +\ L_{Rx})}. \tag{8}$$

(8)

The resulting expression is a general information model for any wireless channel with a mechanism for retransmission of packets when registering errors. The bandwidth of the channel can be expressed via the signal strength at the receiver input [13].

$$V_{pl} = \Delta F \log_2 \left(\frac{P_{Rx}}{(P_n + P_i)} + 1 \right), \quad (9)$$

where P_{Rx} – signal strength at the receiver input; P_n – a noise level in the channel; P_i – the level of interference noise.

Taking into account [9], signal/noise is the ratio of the energy of the signal E to transmit one bit of information to the noise power density, the following expression can be formed:

$$\frac{E_b}{N_0} = \frac{P_{Rx}}{P_n + P_i} \cdot \frac{\Delta F}{V_{ef}}, \quad (10)$$

where ΔF – the band of the frequency channel; N_0 – the power of white noise in the channel; E_b – the energy to transmit one bit of information.

Then, the bandwidth can be established by the expression:

$$V_{pl} = \Delta F \log_2 \left(\frac{V_{ef} E_b}{\Delta F N_0} + 1 \right). \quad (11)$$

3. DEVELOPMENT OF INFORMATION MODEL OF WIRELESS CHANNEL IN 802.11 STANDARD

To develop an information model of a wireless channel by 802.11 standard, we consider transferring the information in terms of the application layer. Then, first of all, the condition of information exchange without changes and transformations must be fulfilled. After that, for the standard 802.11 channel, information transfer will consist of two stages. Let us consider them on the basis of the complete cycle of transfer of information block DU (Data Unit) between applications at the application level, the scheme of which is shown in Fig. 1.

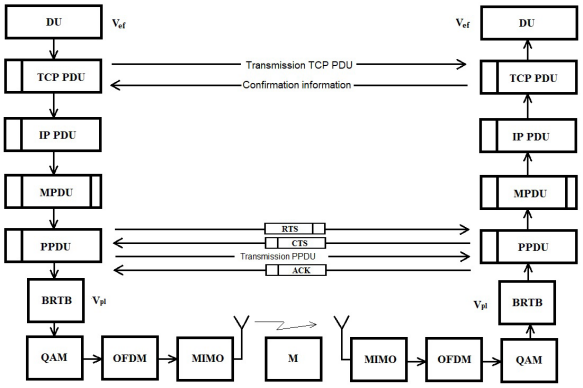

Fig. 1. The scheme of one cycle of transmission of DU block.

The first stage implies formation of DU data blocks and their transmission in a virtual channel. The DU itself is a useful piece of information used by applications. DU length can be specified by the parameter *L*. The time of the DU passing through the transmission path from one application to another per unit of time will determine the efficiency ratio of transmission of information. To transmit this block in channels and networks, there are PDAs (Protocol Data Units) that contain the service information of the transfer protocol. The most common is the TCP/IP protocol stack that adds the service information to the DU, which can be specified by length $L_{s.TCP}$ and $L_{s.IP}$. The TCP protocol has a duplex packet transfer mode with reliability control mechanism [14]. This implies a link in the reverse direction of the service information confirming receipt of the package, and in case of an error, the overwrite is done. Therefore, the amount of information per packet cycle can be written as follows:

$$L_{TSP/IP} = L + L_{s.TCP} + L_{s.IP} . \quad (12)$$

The second stage involves transferring the data packet via the media (M) using the hardware-software tools for creating a wireless channel at the channel and physical layers [13]. The data packet is transmitted using internal information unit called the frame.

The frames in 802.11 standard are formed at the channel layer and are called MSDU (Mac Service Data Unit). They are customizable by the size of the PDU and $L_{TCP/IP} = L_{MSDU}$. MSAs are added to the MSDU to provide service information by generating MPDU (Mac Protocol Data Unit) frames [15]. Thus, the amount of information in one frame can be determined by expression (13), where $L_{s.MPDU}$ – the length of the service information in the frame MPDU; L_{MSDU} – the length of MSDU frame.

$$L_{MPDU} = L_{s.MPDU} + L_{MSDU} = L + L_{s.MPDU} + L_{s.TCP/IP} . \quad (13)$$

Let us consider the AMPDU aggregation as applied directly to the 802.11 standard. AMSDU aggregation is inappropriate because, in the presence of even a small number of destabilizing factors, there will be a large number of errors in frames for high-speed modes. Thus, the amount of information, taking into account the cycle of transmission, is defined as follows:

$$v_s = L_{RTS} + L_{s.PPDU} + mL_{MPDU} + L_{CTS} + L_{ACK} , \quad (14)$$

where L_{RTS} – the length of the RTS frame; $L_{s.PPDU}$ – *PPDU* service information, including preamble and header; L_{CTS} – the length of the CTS frame; L_{ACK} – the length of the confirmation frame; m – the number of MPDU frames in the aggregated frame of the AMPDU.

The time required to transmit the amount of information in the channel, taking into account service information and delays for the full frame of transmission MPDU, can be written as follows:

$$t_s = t_{Difs} + t_{BO} + t_{RTC} + t_{Sifs} + t_{CTS} + t_{Sifs} + t_{MPDU} + t_{Sifs} + t_{ACK} + 2t_{ds}, \quad (15)$$

where t_{BO} – delays in selecting time slots to prevent collisions; $t_{Difs,}$ t_{Sifs} – inter-frame delay and small intercity delay, respectively; t_{RTS} – RTS frame transmission time; t_{CTS} – time of transmission of CTS frame; t_{MPDU} – time of transmission of MPDU frame; t_{ACK} – time of transmission of the ACK frame; t_{ds} – the time delay of the signal.

According to the specification of 802.11 standard [13], the delay for choosing time slots can be determined as follows:

$$t_{BO} = random(0, CW\ \min) \cdot T_{st}, \quad (16)$$

where *random ()* – a random function of choosing the size of the window of the conflict to prevent overload and collisions in the channel; T_{st} – the length of the time interval in CSMA/CA.

The time of transmission of the information frame will be (17), where $t_{s.PPDU}$ – service information containing a preamble and a physical level (layer) heading.

$$t_{MPDU} = t_{s.PPDU} + \frac{m \cdot L_{MPDU}}{V_{pl}}. \quad (17)$$

Frame transfer time RTC, CTS and ACK can be defined as follows:

$$t_{RST} = t_{s.PPDU} + \frac{L_{RTS}}{V_{pl}}, \quad (18)$$

$$t_{CTS} = t_{s.PPDU} + \frac{L_{CTS}}{V_{pl}}, \quad (19)$$

$$t_{ACK} = t_{s.PPDU} + \frac{L_{ACK}}{V_{pl}}. \quad (20)$$

There are also some delays associated with the formation and transmission of the signal in the environment. After transforming the PPDU frame into a bit sequence in the BRTB (Bit Rate Transform Block), it is possible to select a certain group of delays. Thus, we can write:

$$t_{ds} = t_{QAM}^{Tx} + t_{OFDM}^{Tx} + t_{MIMO}^{Tx} + t_{sp} + t_{QAM}^{Rx} + t_{OFDM}^{Rx} + t_{MIMO}^{Rx} + 2t_{PMD}, \quad (21)$$

where t_{QAM}^{Tx} – the delay in the transmitter modulator; t_{OFDM}^{Tx} – the delay in forming OFDM; t_{MIMO}^{Tx} – the delay to the formation of spatial flows MIMO; t_{sp} – the delay of the signal passing in the medium of transmission; t_{MIMO}^{Rx} – the delay for the integration of spatial flows MIMO; t_{OFDM}^{Rx} – the delay on the inverse transform of OFDM; t_{QAM}^{Rx} – the delay in receiver demodulator; t_{PMD} – the delay for converting a frame to a bit sequence at the PMD sublevel.

Taking into account the useful information in the loop and the time it passes through the wireless channel of the 802.11 standard, the efficiency factor will look like this:

$$K_{ef} = \frac{m(L_{MSDU-\,L_{s.TCP/IP}})}{(t_{Difs} + t_{BO} + 3t_{Sifs} + 4t_{s.PPDU+t_{ds}})V_{pl+L_{RTS}+L_{CTS}+mL_{MPDU+\,L_{ACK}}}}. \quad (22)$$

The resulting expression is an information model of a wireless channel of the 802.11 standard and provides an opportunity to evaluate the efficiency of the transmission of the DU information block in the absence of errors in frames. The amount of information in the TCP protocol when errors occur in the virtual channel will be (23), where *n* – the number of packet reload cycles in case of errors.

$$L_{TCP/IP} = L + L_{s.TCP} + L_{s.IP} + \sum_{i=1}^{n}(L + L_{s.TCP} + L_{s.IP})_i. \quad (23)$$

The 802.11 standard has a mechanism that defines the number of retransmission requests for well-received frames and the number of well-received frames, where the request for retransmission was sent more than once. Thus, each retransmission cycle is the transmission of the MPDU information frame using the RTS/CTS loop. In this case, it is expedient to apply a period of estimation *T*, for which a certain number of frames without error N_f and number of frames with errors N_e will be transmitted (24). Then, using expressions (3) and (4) the efficiency of the wireless channel 802.11, taking into account frames with errors, can be determined by expression (25).

$$N = \int_0^T (N_f + N_e)dt\,. \quad (24)$$

$$K = \frac{N_f}{N_f + N_e} K_{ef}\,. \quad (25)$$

The number of frames with errors can be determined by the probability of a bit error [9]. Then the probability of receiving an error frame can be determined as follows:

$$P = 1 - (1 - p)^{v_c}\,. \quad (26)$$

Considering (26) and (5), we can write it as follows:

$$K_{ef.e} = \frac{K_{ef}}{2 - (1 - p)^{v_c}}\,. \quad (27)$$

The resulting expression takes into account the transmission of the frame for an individual mode of the channel operation when one radio is present in the network. 802.11 standard networks provide more than one subscriber, while they all exchange frames on one frequency channel. The efficiency of the 802.11 standard channel, taking into account the number of subscribers on the network, can be described as follows:

$$K_{ef} = \frac{m(L_{MPDU} - L_{s.MPDU} - L_{s.TCP/IP})}{2 - (1-p)^{V_c} \sum_{i=1}^{k} \gamma_i \left(\left(t_{RTS/CTS} + t_{sc} \right) V_{pl} + L_{RTS} + L_{CTS} + mL_{MPDU} + L_{ACK} \right)}, \quad (28)$$

where $t_{RTS/CTS}$ – time frame transmission in the RTS/CTS cycle; t_{sc} – time of scanning of time slot by a subscriber; γ_i – the probability of receiving a frame from k-th participant in the network.

4. ANALYSIS OF RESEARCH RESULTS

The reliability of the obtained models can be verified by mathematical modelling and compared with the results of experimental studies [16]–[18]. Starting conditions for modelling are selected based on the capabilities of the 802.11 standard. We can perform the mathematical modelling of the information model (8) taking into account expressions (9) and (11). The results are shown in Fig. 2.

Analysis of the results demonstrates that an increase in the effective rate of information transmission in the channel reduces the information efficiency of the channel, since the probability of frames with errors increases. Energy efficiency shows that when reducing errors in the channel, it is necessary to increase the power at the receiver input. The dependence of energy efficiency on the band of the frequency channel was found to be different from the information one.

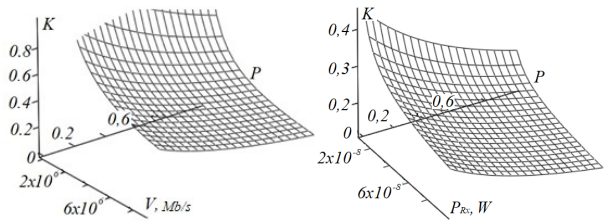

Fig. 2. Channel efficiency: a – information; b – energy.

To analyse the efficiency model for the wireless channel of 802.11 standard, a high-performance mode with aggregation of frames was selected. The results of mathematical modelling are presented in Fig. 3. Frame aggregation is supported in the 802.11n standard and is mandatory for high-performance modes of 802.11ac standard.

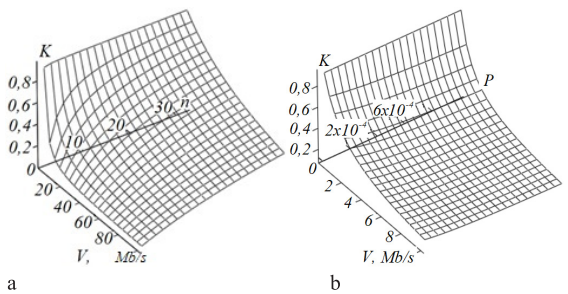

Fig. 3. The ratio of channel efficiency: a – for frame aggregation; b – when receiving frames with errors.

Further, let us consider modelling the efficiency of the channel in the presence of other participants in the network. For this purpose, we will set the maximum loaded mode of the network, in which at the same time everyone is active and forms MSDU frames ($\gamma_i = 1$). From the practical point of view, on average, an access point can support 20–40 users. The results of this simulation are presented in Fig. 4.

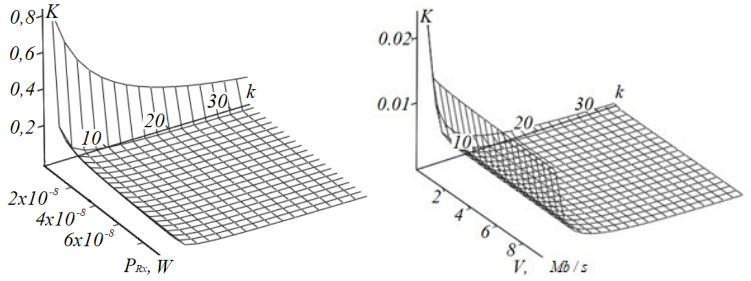

Fig. 4. The dependence of the efficiency of the channel on the number of channels:
a – the signal strength at the receiver input;
b – the effective transmission speed.

The obtained results of the analysis coincide with the experimental research data. Namely, the signal strength level has insignificant changes from the number of participants existing simultaneously. The greater the number of active participants in the network, the lower the effectiveness of the physical frequency channel for a single subscriber. For example, the difference in the efficiency rate of information transmission is more than twice between one and two active participants in the network [16]–[19].

5. CONCLUSIONS

1. The information model of the wireless channel of the 802.11 standard has been obtained taking into account the complete packet and frame transmission cycle. The obtained model provides an opportunity to carry out an assessment of the transfer of useful information for both individual mode and a network of several active participants. This model, unlike the other existing models, takes into account the package construction and frame construction, the technology of aggregation of frames.
2. It has been established that channel efficiency is mostly affected by the presence of destabilizing factors in the channel, which lead to an increase in the number of service information and an increase in the transmission cycle due to the creation of reciprocal queries. It has been confirmed that at the level of signal strength, the number of simultaneously existing participants has little effect in contrast to the effective transmission speed where the impact has a directly proportional dependency.

REFERENCES

1. Barachi, M., Kara, N., Rabah, S., & Forgues, M. (2015). An Open Virtual Multi-Services Networking Architecture for the Future Internet. *Journal of Internet Services and Applications*, *6*(3), 1–22.
2. Mykhalevskiy, D. (2017). Development of a Spartial Method for the Estimation of Signal Strength at the Input of the 802.11 Standard Receiver. *Easten-European Journal of Enterprise Technologies*, *4/9*(88), 29–36.
3. Mussabayev, R.R., Kalimoldayev, M.N., Amirgaliyev, Y.N., Tairova, A.T., & Mussabayev, T.R. (2018). Calculation of 3D Coordinates of a Point on the Basis of a Stereoscopic System. *Open Engineering*, *8*(1), 109–117.
4. Nesterenko, S.A., & Ivanova, L.V. (2011). An Analytical Model of the Pass-Through Channel of the Wireless IEEE 802.11 Network Segment. *Works of Odessa Polytechnic University*, *01*(35), 146–150.
5. Nesterenko, S.A., & Nesterenko, Yu.S. (2015). Analysis of the Bandwidth of the Wireless Channel in the Accelerated Transmission Modes. *East European Magazine of Advanced Technology*, *3/9*(75), 20–24.
6. Kim, H., Park, E.C., Lee, S.K., & Hu, C. (2011). Fast Performance Assessment of IEEE 802.11-based Wireless Networks. *Mathematical and Computer Modelling*, *53*, 2173–2191.
7. Yarilovets, A.V., Nazaruk, V.D., & Zaitsev, S.V. (2014). An Evaluation of the Efficiency of Information Technology for Wireless Access Systems Built on the Basis of Optimal Orthogonal Multi-Frequency Signal Constructions. *Mathematical Machines and Systems*, *2*, 51–58.
8. Amirgaliyev, B.Y., Kenshimov, C.A., Baibatyr, Z.Y., Kuatov, K.K., Kairanbay, M.Z., & Jantassov, A.K. (2015). Statistical Inference in ALPR System. In *9th International Conference on Application of Information and Communication Technologies, AICT 2015 – Proceedings* (pp. 310–313), 25 November 2015, Article number 7338569.
9. Kychak, V.M., & Tromsyuk, V.D. (2017). Assessment Method of Parameters and Characteristics of Bit Errors. *Journal of Automation and Information Sciences*, *49*(5), 59–71.
10. Sharma, R., Singh, G., & Agnihotri, R. (2010). Comparison of Performance Analysis of 802.11a, 802.11b and 802.11g Standard. *International Journal on Computer Science and Engineering*, *02*(06), 2042–2046.
11. Mykhalevskiy, D., Vasylkivskiy, N., & Horodetska, O. (2017). Development of a Mathematical Model for Estimating Signal Strength at the Input of the 802.11 Standard Receiver. *Easten-European Journal of Enterprise Technologies*, *4/9*(88), 38–43.
12. Gorbaty, I.V. (2017). Research of Technical Efficiency of Telecommunication Systems and Networks Using Different Methods of Data Transmission with Feedback Manager. *Information and Control Systems on the Railway Transport*, 1, 18–23.
13. Prokis, D. (2000). *Digital communication*. Moscow: Radio i svyaz'.
14. Insam E. (2003). *TCP/IP embedded internet applications*. Oxford: Elsevier Ltd.
15. Perahia, E., & Stacey, R. (2013). *Next generation wireless LANs: 802.11n and 802.11ac.* Cambridge: Cambridge University Press.
16. Buyankin, V.M. (2018). Neuroidentification With Neuro-Self Tuning to Ensure the Operation of the Current Loop of the Electric Drive with the Desired Static and Dynamic Characteristics. *Periodico Tche Quimica*, *15*(30), 513–520.

17. Mykhalevskiy, D.V. (2018). Construction of Mathematical Models for the Estimation of Signal Strength at the Input to the 802.11 Standard Receiver in a 5 GHz Band. *Easten-European Journal of Enterprise Technologies*, *6/9*(96), 16–21.
18. Mykhalevskiy, D.V. (2019). Investigation of Wireless Channels of 802.11 Standard in the 5GHz Frequency Band. *Latvian Journal of Physics and Technical Sciences*, *1*, 41–51.
19. Mykhalevskiy, D.V., & Horodetska, O.S. (2019). Investigation of Wireless Channels according to the Standard 802.11 in the Frequency Range of 5 GHz for Two Subscribers. *Journal of Mechanical Engineering Research & Developments*, *42*(2), 50–57.

INFORMĀCIJAS MODEĻU ATTĪSTĪBA 802.11 STANDARTA BEZVADU KANĀLA PARAMETRU NOVĒRTĒJUMA EFEKTIVITĀTES PALIELINĀŠANAI

D. M. Mihalevskijs, V. M. Kičaks

K o p s a v i l k u m s

Pētījuma mērķis ir izstrādāt informācijas modeļus, lai uzlabotu bezvadu kanālu parametru novērtēšanas efektivitāti standartā 802.11. Standarta 802.11 bezvadu kanāla informācijas modeli raksturo iespēja novērtēt informācijas bloka pārsūtīšanas efektivitāti, ņemot vērā pilnu pakešu un kadru pārraides ciklu kadru kļūdu rašanās gadījumā. Turklāt modelis atspoguļo citu abonentu esamību tīklā un frekvences kanāla fizisko resursu izmantošanas konkurences mehānismu.

20.09.2019.

sciendo

LATVIAN JOURNAL OF PHYSICS
AND TECHNICAL SCIENCES
2019, N 5

DOI: 10.2478/lpts-2019-0029

OPTIMIZATION OF THE SELECTION METHOD FOR RECONSTRUCTION OF OUTWORN GAS DISTRIBUTION PIPELINE

A. Koposovs, I. Bode, L. Zemite, E Dzelzitis, T. Odineca,
A. Ansone, A. Selickis, A. Jasevics

Riga Technical University,
Faculty of Power and Electrical Engineering, Institute of Power Engineering,
12-1 Azenes Str., Riga, LV-1048, LATVIA
laila.zemite@rtu.lv

Currently, problems related to the operation and exploitation of safe gas distribution networks are deepening in Latvia and Eastern Europe, as the number of outworn underground gas pipelines is steadily increasing. It should be noted that there is a rather wide choice of technology and materials for gas distribution pipeline reconstruction, while at the same time there is no universal method that equally meets all possible work requirements. Therefore, it is an urgent task to understand the operational algorithm, while choosing optimal reconstruction option, classifying and determining the criteria affecting the choice, and determining the scope of each reconstruction method. For this reason, it is necessary to develop a scientifically based methodology for selecting the optimal method for the reconstruction of outworn gas distribution pipelines. Therefore, there are the following tasks that need to be accomplished: to carry out a complex analysis of reconstruction methods and factors determining the choice of an optimal gas distribution pipeline reconstruction method as well as perform the analysis of current state and development of gas supply network; to develop an algorithm for selecting an optimal gas distribution pipeline reconstruction method based on a multi-criteria approach; to develop a mathematical model for the selection of an optimal reconstruction method and scientifically based complex evaluation procedures taking into account technical and economic criteria; to analyse the interaction of the polyethylene gas pipeline with the steel frame during the post-reconstruction process using U-shaped pipe; to develop recommendations for the optimisation of gas distribution network reconstruction programmes. As a result of these tasks, a scientifically justified methodology for the selection of an optimal method for the reconstruction of the gas distribution pipes has been developed.

Keywords: *gas pipelines, mathematical models, optimization, polyethylene pipes, reconstruction*

1. INTRODUCTION

Natural gas distribution systems provide gas transmission to users. The distributing gas pipelines are constructed in urban, village and residential areas. Until 1998, only steel pipes were used to construct gas pipelines, but currently polyethylene tubes are increasingly preferred. Distribution systems include gas regulating equipment, special constructions and pipelines with closing devices, anti-corrosive equipment and other network devices. The total length of the distribution system pipelines in Latvia is 5907.69 km (Table 1).

Table 1

Distribution of Natural Gas Pipeline Construction

Length of pipelines owned by the company (km)		**5,243.15**
High pressure gas pipelines (km)		997.75
Medium pressure gas pipelines (km)		1,848.89
Medium pressure gas pipelines 100 mbar (km)		332.52
Low pressure gas pipelines (km)		2,063.98
Not owned by the company (km)		**820.01**
Length of pipelines carried out by the company (km)		**5,907.69**
Owned by gas operator (km)	Steel pipelines	3,292.64
	Polyethylene pipelines	1,950.51
Not owned by gas operator (km)	Steel pipelines	203.53
	Polyethylene pipelines	616.48

The technical operation of the distribution pipeline systems is carried out by the distribution system operator (DSO). The lifetime of the operating steel and polyethylene pipelines is given in Table 2 according to 01.01.2019 data. Certain complex and highly qualified works are carried out by the distribution system operator's special services (e.g., gas pipeline diagnostics, etc.).

Table 2

Lifetime of Operational Steel Pipelines

Gas pipeline material	**Lifetime of operational pipelines, years**						**TOTAL**
	below 10	10–20	20–30	30–40	40–50	above 50	
Polyethylene, km	**324.24**	**1445.44**	**140.32**	**40.66**	**0.00**	**0.00**	**1950.66**
Amount, %	17	74	7	2	0	0	
Steel, km	**30.23**	**244.43**	**729.25**	**985.62**	**846.95**	**456.64**	**3293.12**
Amount, %	1	7	22	30	26	14	
TOTAL	**354.47**	**1689.86**	**869.57**	**1026.28**	**846.95**	**456.64**	**5243.78**

Results of the analysis of the development phases of Latvian pipeline systems allowed identifying changes in gas distribution network over the past 25 years; it also allowed determining the current state of the network, taking into account the lifetime of pipelines, as well as the level of gasification achieved in the regions and defining the possibilities of using polyethylene pipes and the required gas distribution pipe reconstruction amount. Since the steel pipelines are not constructed in a single

year, they are operated with a variety of time, depreciation and other factors, which require different technical operations and renovations.

The assessment of the technical state of the natural gas transmission pipeline system (*P>16 bar*) has been studied by A. Borodiņecs, A. Broks, A. Dāvis, A. Ješinska, A. Krēsliņš. Natural gas distribution networks (*P<16 bar*) have been studied in the recent years [1]–[6].

2. METHODOLOGY FOR ASSESSING THE TECHNICAL STATE OF THE PIPELINE AND SETTING THE CONDITIONS FOR FUTURE OPERATIONAL FEASIBILITY

The methodology for assessing the technical state of the distribution pipeline systems and determining the conditions for future operational feasibility was developed according to the algorithm developed in the study (Fig. 1).

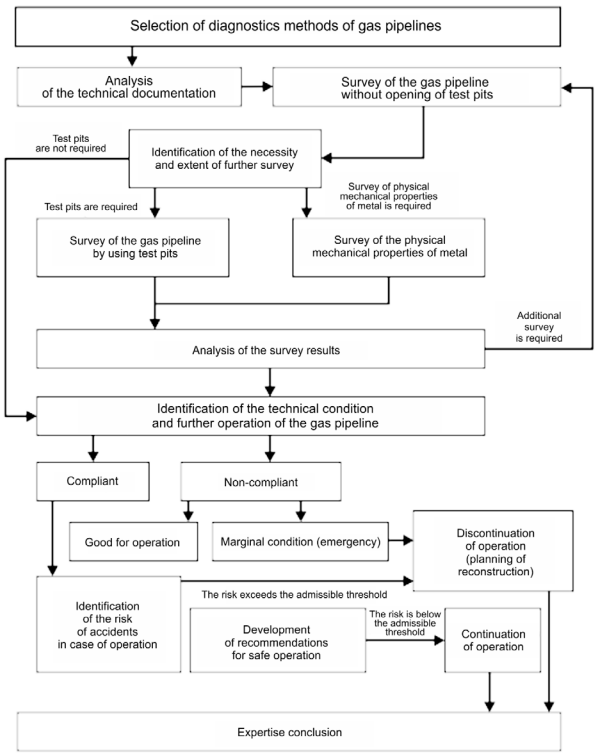

Fig. 1. Algorithm for performing underground steel gas pipeline diagnostics.

In order to assess the technical condition, the possibility of non-accidents in the gas pipeline must be calculated. According to the technical state of the pipeline, the probability of non-accident – $H_{i_{BP}}$ for case i shall be calculated using the following relations based on the results of the technical diagnosis, taking into account the found defects and damage ($H_{i_{BP}}$):

$$H_{i_{BP}} = \prod_{s_i=1}^{s_i}\left(1 - k_{\sum} \cdot P(A_i)\right)^{ms}, \quad (1)$$

where $\prod$ – multiplication sign of multiplicators, s_i – number of defects and types of damage; $k_{\sum}$ – correction factor (occurrence of accidents); $P(A_i)$ – probability of occurrence of an accident defect or damage, ms – the number of defects or damage of one type.

After the prevention of any defects and damage ($H_{i_{AP}}$) detected during the survey, taking into account defects and damage, which have not been observed for objective and subjective reasons it is possible to calculate:

$$H_{i_{AP}} = \prod_{s_i=1}^{s_i}\left(1 - k_{\sum} \cdot P(A_i)\right)^{L_s}, \tag{2}$$

where L_s – the number of failures and/or damage, which were not observed.

$k_{\sum}$ for the hazards of defects and damage equal to the multiplication of individual factors k_i:

$$k_{\sum} = \prod_{i=1}^{n} k_i, \tag{3}$$

where n – the amount of correction factors k_i, i – the number of individual factor. L_s can be calculated using (4):

$$L_s = ms \cdot \left(\frac{(1 - P_{d-op}}{P_{d-op}}\right), \tag{4}$$

where P_{d-op} is defectoscope operator probability of finding a defect or damage. Probability of occurrence of an accident defect or damage and correction factor (occurrence of accidents) for the hazards of defects and damage is determined on the basis of statistical data on accidents and incidents on gas pipeline, and it is equal to:

$$P(A_i) = \frac{1}{N \cdot AK_i}, \tag{5}$$

where $N \cdot AK_i$ – the average occurrence of specific type defects on the gas pipeline per accident, on one kilometre of the pipeline within one year. Correction factors k_i can be calculated by (6):

$$K_i = k_b \cdot \frac{N_i}{N_{min}}, \tag{6}$$

where k_b – the weight factor of the operating conditions, taking into account the varying influence of different impact groups of operation; N_i and N_{min}– i – minimum incidence of defects in one of the operating condition groups.

The correction factor k_i for the hazards of defects and damage allows taking into account characteristics of the gas pipeline and operational influence on the hazard level of defects and damage (Table 3).

Table 3

Values of the Danger Adjustment Coefficients of Defects and Damage of the Gas Pipeline

Characteristics of an underground pipeline		k_i (eventual)
Operational conditions		
Type	between the village	1.00
	distribution	1.05
	inlet	1.10
Pressure	low	1.00
	medium	1.05
	high	1.10
The route of the gas pipeline across natural and artificial obstacles	none	1.00
	a water obstacle	1.05
	a road or a railway	1.10
	a road and a railway	1.15
Regulated distances from the gas distribution network	complied with	1.00
	not complied with	1.05
The protection potential is ensured along the whole length or electrical chemical protection, not required		1.00
The protection potential is ensured not along the whole length at a high soil corrosion activity or if there is a dangerous impact of stray		1.10
The protection potential is ensured not along the whole length at a high soil corrosion activity and if there is a dangerous impact of stray currents		1.20
Interruptions in the operation of the electrical chemical protection device exceed permitted terms		1.05

The likelihood of defect is determined:

- based on the characteristics of the used tools and equipment;
- based on the parameters of the gas pipeline;
- based on external factors such as the presence of interference, road surface quality, soil moisture in the area where pipeline lays, etc.;
- based on subjective factors, such as the qualifications of the contractors.

Certain values are determined on the basis of external and subjective factors, but must not exceed the maximum values.

The maximum parameters for the probability of defects and damage are given in Table 4.

Table 4

The Maximum Possibility of Identification of Defects and Damage of Gas Pipelines

Description of the defect section	The maximum possibility of identification of the defect
Penetrating defect	
High pressure	0.98
Medium pressure	0.95
Low pressure	0.90
Low pressure ($d < 1mm$)	0.85
Damage of insulation coating	
Within the territory of an inhabited location	0.70
Within the territory of inhabited locations where there are no connected engineering communications	0.75
Outside an inhabited location	0.80
The lack of adhesion along the whole length of a gas pipeline	0.98
Destruction of the insulation coating along the whole section (the transitional resistance below the critical value), as confirmed for several times by means of test pit surveys	0.99

The values of $P(A_i)$ obtained from the operational statistics of DSO distribution gas pipeline systems are given in Table 5.

Table 5

The Criteria for Assessing the Degree of Danger of Defects and Damage of the Gas Pipeline

Defects and damage of the insulation coating		$\boldsymbol{P(A_i)}$
Mechanical and structural	Damage	0.0050
	Unsatisfactory adhesion in a test pit	0.0015
	The lack of adhesion along the whole length of a section	0.0700
	Transitional resistance in a test pit below the critical value	0.0030
	Destruction of the insulation coating along the whole length of a section	0.0200
Defects and damage of the pipeline metal		$\boldsymbol{P(A_i)}$
Corrosion	Penetrating, $d > 1\ mm$	0.250
	Penetrating, $d < 1mm$	0.1500
	Local (ulcer, point)	0.0600
	General, the remaining thickness of wall below 70%	0.0350
	General, the remaining thickness of wall between 99% and 70%	0.0200
Structural	The loss of the pipeline strength	0.5000
	Rupture of a welded joint	0.2500
	Defect of a welded joint $d < 1mm$	0.1500

When determining the number of defects and damage caused by corrosion damage and found in a single viewing area of a size not exceeding 1.5 m, the principle according to which more significant damage covers minor damage should be used.

For example, if both transverse and point damage are detected in the single viewing area, only the transverse one is taken into account. It is assumed that the number of one type of defect per standard size single viewing area 1.5 m is *1*.

The assessment of the technical condition is carried out on the basis of the boundary status criterion, the probability of non-accident is equal to 0.95. Based on the diagnostic results of the gas pipeline, its condition can be evaluated as technically appropriate, operational or boundary. Depending on the probability of non-accident occurrence, developed and recommended time extensions of the safe operating period of the gas pipeline are specified in Table 6.

Table 6

Recommended Extensions of Lifetime

The possibility of non-emergence of accidents, $H_{i_{AP}}$	Recommended term of safe operation, years, up to
0.990 – 1.000	10
0.980 – 0.990	9
0.975 – 0.980	8
0.970 – 0.975	7
0.967 – 0.970	6
0.964 – 0.967	5
0.960 – 0.964	4
0.955 – 0.960	3
0.950 – 0.955	2
≤ 0.950	1

A gas pipeline whose technical condition is recognised as a boundary state ($H_{i_{AP}} < 0.950$) must be decommissioned, reconstruction or refurbishment of the pipeline must be carried out. A gas pipeline whose condition is recognised as operational ($H_{i_{AP}} < 0.950$) is considered fit for operation if safe operation measures are implemented. If, despite the detection of defects, according to diagnostic results and calculations, probability of non-accident until their elimination exceeds 0.950 and the gas pipeline can be declared operational, these defects shall be considered as repairable.

From the economic indicator aspect, the dominant method of reconstruction is the one where polyethylene pipes are laid in without degrading the steel pipeline. In addition, the impact of the territorial area of construction indicator, takes into account the density and nature of the buildings in areas where gas pipes are laid.

Advantages of the reconstruction method with pipe laying without pre-degradation are the following: simplicity of construction works; cheapness of technology; the possibility of using standard polyethylene pipes and coupling parts; complete refusal of electrochemical protection installation. Disadvantages are limits of strength reserve coefficient; difficult gas leak detection; significant reduction in flow and relatively low load-bearing capacity. Advantages of the reconstruction method with pipe laying with pre-degradation are the following: the possibility of replacing the pipes with the same or greater diameter pipes; there is no need to clean the pipeline before; with polyethylene pipes, the reconstructed section does not require standard polyethylene pipes. Disadvantages are that it is necessary to

make reinforced pipes; significant constraints in the case of engineering networks, expenditure related to the Environmental Impact Assessment; small length of reconstructed pipeline sections and pipe curves make work difficult. Advantages of reconstructing a tightly sealed pipe (U-type) are the following: minimal reduction in pipeline diameter; permeability is not limited; no need for standard polyethylene pipes in reconstructed pipeline. Minuses are that careful inspection and cleaning of the old pipelines are needed; additional equipment for special pipe handling and trained personnel is required; pipe diameter and pressure limits and refitting are necessary. Advantages of the reconstruction by using synthetic pipe branch are the following: minimum equipment required; it is possible to reconstruct long pipelines; the possibility to reconstruct the gas pipelines at a pressure of up to 1.2 MPa. Disadvantages are that it is possible to break the pipe branch in the reconstruction process; after the reconstruction, the steel pipeline may require protection using standard polyethylene pipes; relatively expensive technology; careful cleaning of the old pipe needs to be done. Advantages of "primus line" [6] method are high permissible load; high flexibility; high efficiency; non-significant impact on landscape and protected areas; possibility to perform recovery of long pipelines with sharp turns. Disadvantages are high costs of the technology; there are not many large-scale entrepreneurs who could implement this type of technology and due to the inaccuracy of the tractive force calculation, it is possible to break the pipe branch during the laying process. Advantages of the open reconstruction method are that there are no temperature or other limits for the performance of works; a potential increase in pressure in a new city where an increase in gas consumption is likely to occur. Disadvantages are high costs of the technology; high environmental pollution; long duration of work; disruption of transport movement at work site.

The analysis of the existing European legislation confirmed the need to take this indicator into account in the process of choosing the optimal gas distribution pipeline reconstruction option, as the task associated with optimum reconstruction is linked to many factors. This task should be based on high-quality engineering research and diagnostic research data, safety requirements and evaluation of existing regulatory framework [7]–[10].

3. ALGORITHM FOR SELECTING RECONSTRUCTION METHOD FOR OUTWORN GAS DISTRIBUTION PIPELINES

As a result of the above-mentioned research and methods, the algorithm and methodology for choosing the optimal method for the reconstruction of the outworn gas distribution pipes have been developed (Fig. 2), based on a multi-criteria approach.

The methodology developed is implemented in the following phases: collecting information – identification of feasible solutions – appointing experts and expert groups – determination of comparison criteria – identifying questions and drawing up questionnaires – analysis of expert assessments – determination of competence coefficients – multi-factor analysis mathematical model calculation – comparing alternatives – choice of optimal method. The study, on the choice of an

optimal reconstruction method, proposes an approach based on two sets of criteria: technical and economic. The following criteria have been adopted using analysis as well as technical documentation, with the greatest impact on the selection of an optimal reconstruction option (Table 7).

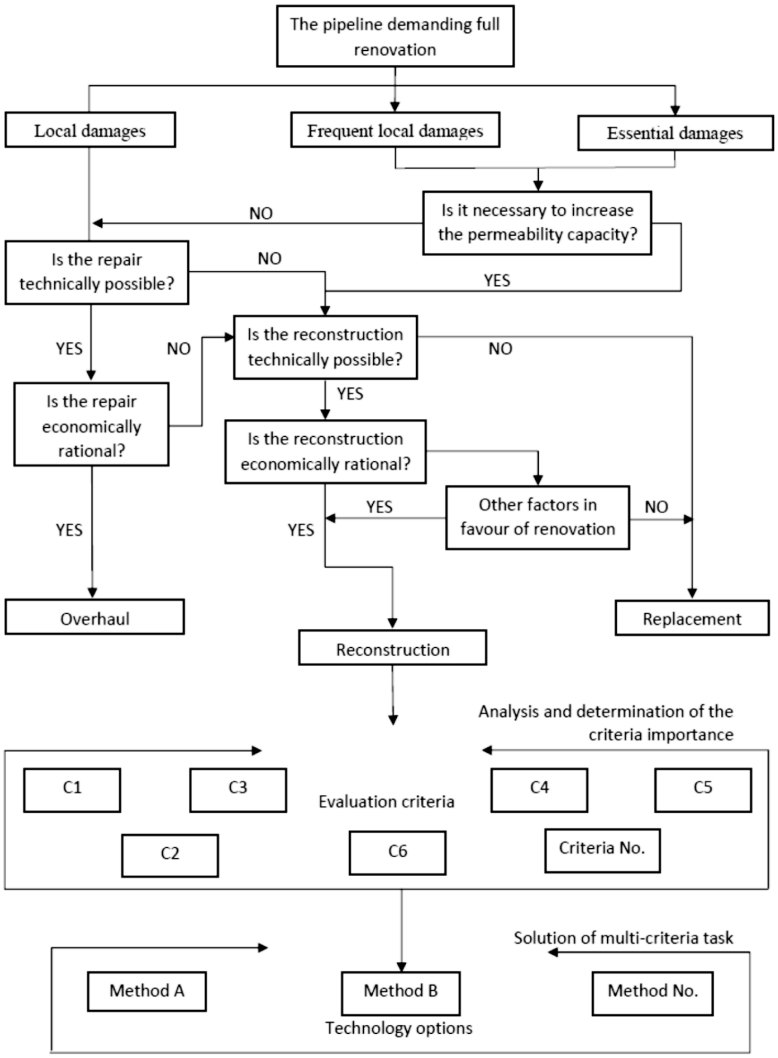

Fig. 2. Algorithm for choosing the optimal reconstruction method.

Based on criteria and the expert analysis questionnaire, assessment and data collection were done in order to create a mathematical model. Taking into account specific calculated competence coefficients and factor importance coefficients, a group calculation was performed for each reconstruction method. The results and calculations of engineers in the program complex *Expert Choice* indicated that reconstruction for outworn gas distribution pipe, by using a method with tightly attached pipe, might be considered optimal when assessed from the perspective of technical criteria.

Table 7

Criteria for Assessment

Comparison criteria	**Symbol**
Technical criteria	
Gas pipeline operating pressure	C1
Degree of preparedness of reconstructed gas pipeline (volume of works and extent of clarification of internal space)	C2
Volume of earthwork	C3
Diameter of reconstructed gas pipeline	C4
Frequency of occurrence of emergency situations in case of the relevant method	C5
Level of restrictions of the transport movement intensity	C6
Necessity of electrochemical protection	C7
Land allocation area for the period of construction and assembly work	C8
Degree of complexity of quality control	C9
Possibility of use of the standard equipment	C10
Territorial area of work	C11
Permissible length of the reconstructed gas pipeline stage	C12
Economic criteria	
Construction costs	C13
Internal rate of return	C14
Net discounted profit	C15
Profit index	C16
Repayment duration	C17
Duration of construction and assembly work	C18

4. OPTIMAL SEQUENCE OF RECONSTRUCTION PROJECT IMPLEMENTATION

Applying the optimal sequence of implementation of reconstruction projects allows determining the order in which reconstruction should be done, taking into account the technical condition and financial constraints of the distribution network stations. To determine the degree of depreciation and the technical condition of the gas distribution pipelines, it is proposed to perform the planned reconstruction in the following stages: functional diagnostics and risk analysis of complex technical diagnostics. According to the results of functional diagnosis, the technical condition of the gas distribution system object may be recognised as:

- valid for work; condition of the site is described as free of defects and damage that affects the bearing capacity and operational validity;
- valid for work; condition in which several assessable parameters do not comply with the requirements or norms of the project, but this non-compliance with the requirements does not lead to working disruption and the bearing capacity of construction is ensured, taking into account the effects of existing defects and damage;
- inoperable; the condition of the object, in which characterising ability of at least one parameter, to perform the specified functions, does not meet the regulatory technical and/or project requirements.

If an object is found to be inoperable or if hidden defects are detected during functional diagnosis, it is necessary to perform a complex technical diagnosis of the site. A summary of implementation of the technical status assessment and reconstruction projects is proposed based on a comparison of the risk indicators with an acceptable risk. In order to carry out an overall risk assessment of gas distribution network objects, it is proposed to confirm the expected loss due to the accident, determining the amount of specific losses in monetary terms, which is not limited only to a qualitative risk analysis. Optimal allocation of funds through the implementation of the reconstruction program is an important task of reconstruction of objects because it allows providing a certain financial effect in the circumstances where financial constraints are imposed. The solution for the specific task is proposed by using the dynamic programming method.

5. CONCLUSIONS

Studies of existing methods for the reconstruction of outworn gas pipelines have allowed identifying and systemising the main advantages and disadvantages of each method, as well as identifying criteria that influence an optimal selection of the method. It should be noted that the task of selecting an optimal reconstruction method is a multi-factor one. The developed concept allows determining the optimal method of reconstruction of gas distribution pipeline taking into account technical and economic criteria. Technical feasibility has been demonstrated for the use of polyethylene pipes in the reconstruction of gas pipes designed for 1.2 MPa operation together with a steel frame, the role of which is fulfilled by a renewable steel gas pipeline. The developed recommendations and algorithm allow determining an optimal sequence for the implementation of reconstruction projects taking into account both the technical state of the pipelines and the financial constraints.

ACKNOWLEDGMENTS

The research has been supported by the National Research Programme, project: Trends, Challenges and Solutions of Latvian Gas Infrastructure Development (LAGAS) (No. VPP-EM-INFRA-2018/1-0003).

REFERENCES

1. Bode, I., Laube, I., & Platais, I. (2013). Technical Condition. Assessment of the System of Gas Distribution Pipelines. *Scientific Journal of RTU. 14 series, Būvzinātne*, 6 p.
2. Bode, I. (2014). Sadales gāzesvadu sistēmu tehniskā stāvokļa novērtēšanas metodoloģija. Promocijas darbs. R.: RTU Izdevniecība.
3. Zemīte, L., Kutjuns, A., Bode, I., Kuņickis, M., & Zeltiņš, N. (2018). Risk treatment and system recovery analysis of gas system of gas and electricity network of Latvia. *Latvian Journal of Physics and Technical Sciences*, *55*(5), 3–14. ISSN 0868-8257. DOI: 10.2478/lpts-2018-0031

4. Zemīte, L., Kutjuns, A., Bode, I., Kuņickis, M., & Zeltiņš, N. (2018). Consistency analysis and data consultation of gas system of gas-electricity network of Latvia. *Latvian Journal of Physics and Technical Sciences, 55*(1), 22–34. ISSN 0868-8257. DOI:10.2478/lpts-2018-0003
5. Zemite, L., Bode, I., Zeltins, N., Kutjuns, A., & Zbanovs, A. (2018). Analysis of the power system damage hazard from the point of view of the gas supply system. In: *2018 IEEE International Conference on Environment and Electrical Engineering and IEEE Industrial and Commercial Power Systems Europe, EEEIC/I and CPS Europe 2018*, art. no. 8494380. ISBN: 978-153865185-8, DOI: 10.1109/EEEIC.2018.8494380
6. Primusline. (n.d.) Available at https://www.primusline.com/primus-line/
7. Praks, P., Kopustinskas, V., & Masera, M. (2015). Probabilistic modelling of security of supply in gas networks and evaluation of new infrastructure. *Reliability Engineering and System Safety, 144,* 254-264, DOI: 10.1016/j.ress.2015.08.005
8. Ministry of Economics of the Republic of Latvia. (n.d.). *Doing business evaluation of national gas markets, report for regional gas market coordination group*.
9. Chala, G.T., Aziz, A.R.A., & Hagos, F.Y. (2018). Natural gas engine technologies: challenges and energy sustainability issue. *Energies, 11*(11), art. no. en11112934. DOI: 10.3390/en11112934
10. Miedema, J.H., Van Der Windt, H.J., & Moll, H.C. (2018). Opportunities and barriers for biomass gasification for green gas in the dutch residential sector. *Energies, 11*(11), art. no. en11112969. DOI: 10.3390/en11112969

NOLIETOTU GĀZES SADALES VADU ATJAUNOŠANAS METODES IZVĒLES OPTIMIZĀCIJA

A.Koposovs, I. Bode, L. Zemīte, E Dzelzītis, T. Odiņeca, A.Ansone, A.Selickis, A.Jasevičs

K o p s a v i l k u m s

Rakstā apskatīta zinātniski pamatota optimālas nolietotu gāzes sadales vadu rekonstrukcijas metodes izvēles metodika, balstīta uz multi-kritēriju pieeju, un dotas rekomendācijas gāzes sadales tīkla rekonstrukcijas programmu optimizācijai. Tās var risināt problēmas, kas saistītas ar drošas gāzes sadales tīklu darbības un ekspluatācijas nodrošināšanu, jo Latvijā pastāvīgi palielinās nolietoto pazemes gāzes vadu skaits.

05.08.2019.

sciendo

LATVIAN JOURNAL OF PHYSICS
AND TECHNICAL SCIENCES
2019, N 5

DOI: 10.2478/lpts-2019-0030

MECHANISMS OF ELECTRON SCATTERING IN UNIAXIALLY DEFORMED SILICON SINGLE CRYSTALS WITH RADIATION DEFECTS

S.V. Luniov[1], V.V. Lyshuk[1], V.T. Maslyuk[2], O.V. Burban[3]

[1]Lutsk National Technical University, 75 Lvivska Str., 43018 Lutsk, UKRAINE
[2]Institute of Electron Physics NAS of Ukraine, 21 Universitetska Str., Uzhghorod 88017, UKRAINE
[3]Volyn College of the National University of Food Technologies, 6 Cathedral Str., 43016 Lutsk, UKRAINE
e-mail: luniovser@ukr.net

Temperature dependencies for Hall mobility of electrons for the uniaxially deformed n-Si single crystals, irradiated by the flow of electrons $\Omega=1\cdot10^{17}$ el./cm^2 with the energy of 12 MeV, are obtained on the basis of piezo-Hall effect measurements. From the analysis of these dependencies it follows that under the uniaxial pressure (0–0.42) GPa and (0–0.37) GPa along crystallographic directions [100] and [111], respectively, the deformation-induced increase of the Hall mobility has been observed. On the basis of the proposed theoretical model of mobility, this increase is explained by the decrease of the amplitude of a large-scale potential with an increase in the magnitude of uniaxial deformation and, accordingly, the probability of electron scattering on this potential. The slight discrepancy between the obtained experimental results and the relevant theoretical calculations at the low temperatures is due to the fact that the electron scattering on the radiation defects, created by the electron radiation, was not taken into account in the calculations. The decrease in Hall mobility of electrons along with an increase in temperature for unirradiated and irradiated silicon single crystals is explained by the growth of the probability of electron scattering on the optical phonons that are responsible for the intervalley scattering in silicon. The obtained results can be used in designing and modelling on the basis of n-Si single crystals of various electronic devices of micro- and nanoelectronics, which can be subject to the extreme conditions of action of the significant radiation and deformation fields.

Keywords: *hall mobility, large-scale potential, piezo-Hall effect, uniaxial deformation*

1. INTRODUCTION

Monocrystalline silicon is a promising material for micro- and nanoelectronics thanks to the well-designed technology of its growing and relatively low cost [1]–

[7]. It is known [7] that the traditional control of the electrical properties of silicon or other crystalline semiconductors is carried out by doping with various impurities that create in the band gap of semiconductor the discrete energy levels of the necessary depth and concentration. But often this method is difficult to implement due to the low solubility of the necessary impurities in semiconductors at higher concentrations of the electrically active intrinsic defects or the absence of such impurities at all. Solving this problem is possible by using the method of radiation technologies [8]–[10]. This way, the formation of radiation defects in solids in the integrated combination with other effects such as temperature, mechanical load, the presence of an external electric and magnetic field, and the illumination allow purposefully regulating by the properties of solid-state materials. As it is known [11]–[14], the defects in silicon caused due to irradiation can play a role of various active centres (donors or acceptors that change the concentration of charge carriers and the position of the Fermi level, scattering and recombination centres that affect the electron and hole mobility, life time of non-equilibrium charge carriers). Radiation changes of the electrophysical properties of silicon practically for all temperatures are determined by secondary defects (complexes of vacancies and interstitial atoms with each other, with atoms of chemical impurities) or clusters of defects [12], [14]. Since the basic properties of silicon are strongly dependent on the presence of the defective structure, this, in turn, will have an impact on the parameters of the finished devices manufactured on its basis, such as sensitivity, current amplification factor, response time, stability, selectivity, dark current, etc. [15]–[17]. Designing and modelling on the basis of silicon of the radiation-resistant pressure sensors, which are used in the aerospace, rocket and space industries, thermonuclear and nuclear energy [18]–[20], and of the strained heterostructures, which can be applied in the fields of high radiation [21]–[23], require the detailed research of the impact of radiation irradiation and deformation on the electrical properties of silicon. In most of the works, only the effect of radiation or deformation on the physical properties of silicon single crystals has been considered. But integrated investigations of the effect of radiation and deformation on the electron transfer phenomena in silicon have not practically been carried out. Therefore, in this paper, the impact of high-energy electron irradiation on the electrical properties of uniaxially deformed single crystals n-Si is investigated.

2. EXPERIMENTAL RESULTS

The investigated silicon single crystals with a resistivity of 0.25 Ω·cm, doped with an impurity of phosphorus, concentration of N_d=2.2·10^{16} cm^{-3}, were grown at the Department for Development and Fluctuation Analysis of Semiconductor Materials and Structures of the V.E. Lashkaryov Institute of Semiconductor Physics, NAS of Ukraine. Samples of such silicon single crystals were irradiated by the electron flow Ω=1·10^{17} el./cm^2 with energy of 12 MeV. Silicon single crystals were irradiated at room temperature at the microtron M-30, whose parameters make it possible to form the beams of accelerated electrons with energies in the range of 1–25 MeV with monoenergy of 0.02 % and current of up to 50 μA. Temperature control was executed using a copper-constantan differential thermocouple. During the irradiation,

temperature of the silicon samples was regulated by blowing with vapours of liquid nitrogen. We measured the temperature dependencies of the Hall constant and the electrical conductivity for uniaxially deformed n-Si single crystals irradiated by the electrons. Uniaxial deformation and electric current through the silicon sample were directed along crystallographic directions [100] and [111]. Silicon samples for such research were cut in the form of rectangular parallelepipeds, 0.8·0.8·10 mm in size.

After appropriate preparation, the investigated sample was immovably fixed in brass pins using epoxy resin and placed in a thick-walled stainless steel tube. A small slot was made in the tube for output of the conductors, soldered to the current and Hall contacts of the sample. From below, the sample was supported by the pillar, which was a ceramic cork held by the corkscrew propeller. The tube was vertically attached to the casing with the help of the steel collet, which was installed in the casing. The volume hollow cylinder carried the main load containing a tube in a fixed vertical position. The upper surface of this cylinder had a thread tightened on the tube, and the lower one rested on the casing. A mechanical load was applied to the sample using a ceramic tube, which was inserted into a thick-walled stainless steel tube. A steel rod rested on the ceramic tube. The force was transferred to the steel rod and respectively to the ceramic tube and the investigated sample using the horizontally located lever. A pressure sensor, which was a spring attached to the lever, was used for creation of the mechanical load on the sample. The spring was calibrated in such a way that the certain magnitude of stretching, which was fixed by the vertically posted scale, corresponded to some value of the pressure force on the sample. A reservoir, into which water was served through a tap, was attached to the bottom of the spring. Due to the filling of the reservoir with water, the spring was stretched and the pressure on the sample was increased. The load was removed from the sample by opening the electric valve of the reservoir, which led to the leakage of water and reduced its mass in the reservoir.

Uniaxially deformed sample that was in a thick-walled tube was placed between the poles of the electromagnet, which allowed for a smooth change in the magnetic field within the range from 0 to 0.6 T. The investigated sample was blowing with vapours of liquid nitrogen. The temperature control of samples was carried out also using a copper-constantan differential thermocouple. During the experiment, the accuracy of the measurement of temperature was ±1 K. The measurement error of Hall mobility did not exceed 8 %, and the concentration – 13 %.

In the previous paper [24], on the basis of measurements of infrared Fourier spectroscopy and the Hall effect, the nature and concentration of the main types of radiation defects formed in silicon single crystals under such conditions of irradiation were determined. It was shown that the main radiation defects were A-centres (VO_i complexes), A-centres, modified with impurity of phosphorus (VO_iP complexes) and complexes containing interstitial carbon (C_iO_i complexes).

In order to study the effect of these defects on the electrical properties of uniaxially deformed n-Si single crystals, the authors conducted the research of the piezo-Hall effect at the uniaxial pressures along crystallographic directions [100] and [111] for unirradiated and irradiated samples of silicon.

Figures 1 and 2 present the temperature dependencies of the Hall mobility for unirradiated n-Si single crystals under condition of uniaxial pressure along

crystallographic directions [100] and [111]. As it is well known [25], in silicon single crystals at uniaxial pressure along the crystallographic direction [100] there will be deformation redistribution of electrons between two minima of the conduction band with low mobility, which descend down, and four minima with high mobility, which ascend up on the energy scale. This explains the decrease in the Hall mobility of electrons along with the increasing magnitude of the uniaxial pressure (Fig. 1).

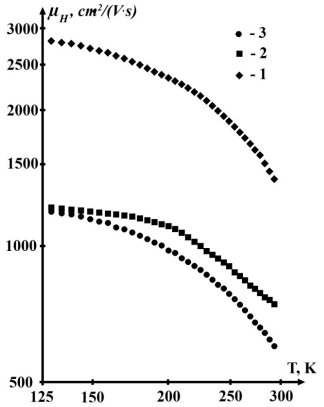

Fig. 1. Temperature dependencies of the Hall mobility for n-Si<P> single crystals at different values of the uniaxial pressure along the crystallographic direction [100]: 1–0 GPa; 2–0.42 GPa; 3–0.83 GPa.

Reduction of the Hall mobility with the increasing temperature is due to the increasing role of electron scattering on optical phonons, which are responsible for the intervalley scattering of electrons in silicon [26]. Detailed investigations of the tensoresistence of n-Si at uniaxial pressure along the crystallographic direction [111] showed that resistivity increased along with a decrease in the electron mobility by increasing the effective mass of electrons at transformation of a two-axis isoenergetic ellipsoid of rotation in the three axes [27]. The increase in the magnitude of tensoresistence of silicon with the increasing temperature in these conditions is explained by the deformation non-parabolicity of the silicon conduction band, which occurs by removing the degeneracy of the zones Δ_1 and Δ_2 at the point X_1 at the edge of the Brillouin zone [27]. These reasons explain the decrease in the Hall mobility of electrons with the increasing magnitude of the uniaxial pressure (Fig. 2).

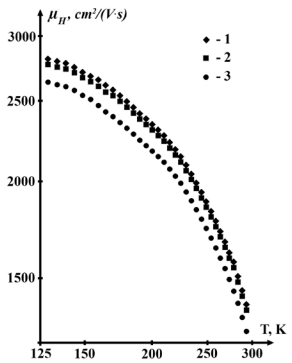

Fig. 2. Temperature dependencies of the Hall mobility for n-Si<P> single crystals at different values of the uniaxial pressure along the crystallographic direction [111]: 1–0 GPa; 2–0.37 GPa; 3–0.74 GPa.

For n-Si single crystals, irradiated by the electrons (see Figs. 3 and 4), the Hall mobility of electrons increases and, reaching its maximum, decreases with the increasing temperature.

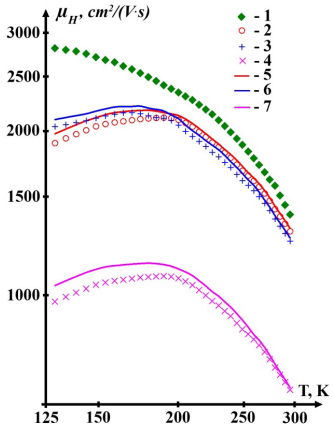

Fig. 3. Temperature dependencies of the Hall mobility for the irradiated n-Si<P> single crystals at different values of the uniaxial pressure along the crystallographic direction [100]: 1–0 GPa (unirradiated sample), 2–0 GPa, 3–0.42 GPa, 4–0.83 GPa. Solid curves are theoretical calculations on the basis of expression (14): 5–0 GPa, 6–0.42 GPa, 7–0.83 GPa.

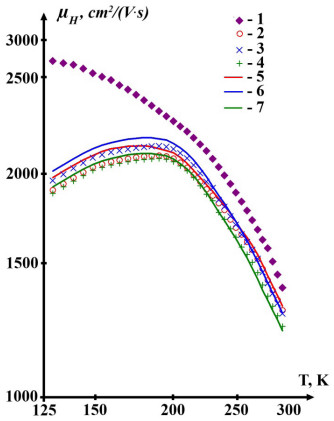

Fig. 4. Temperature dependencies of the Hall mobility for the irradiated n-Si<P> single crystals at different values of the uniaxial pressure along the crystallographic direction [111]: 1–0 GPa (unirradiated sample), 2–0 GPa, 3–0.37 GPa, 4–0.74 GPa. Solid curves are theoretical calculations on the basis of expression (18): 5–0 GPa, 6–0.37 GPa, 7–0.74 GPa.

The growth of the Hall mobility of electrons for undeformed and uniaxially deformed n-Ge single crystals, irradiated by electrons, was explained by the decreasing resistivity gradients due to a decrease in the amplitude of the large-scale potential with the increasing temperature and deformation and also the concentration of charged radiation defects that were the active centres of scattering [28].

The concentration of electrons in the conduction band of irradiated n-Si single crystals was determined on the basis of the piezo-Hall effect measurements at the uniaxial pressures along the crystallographic directions [100] and [111] (Fig. 5).

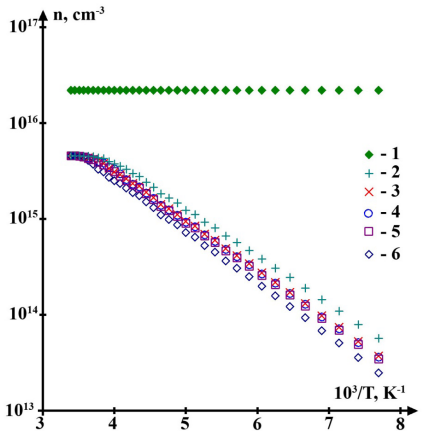

Fig. 5. Temperature dependencies of the concentration of electrons for the irradiated n-Si<P> single crystals at different values of the uniaxial pressure along the crystallographic directions [100] and [111]: 1–0 GPa (unirradiated sample), 2–0.83 GPa ([100]), 3–0.74 GPa ([111]), 4–0.37 GPa ([111]), 5–0.42 GPa ([100]), 6–0 GPa.

According to the data in Fig. 5, the concentration of electrons does not depend on the temperature for the unirradiated single crystals n−Si (both in the absence and in the presence of the uniaxial deformation). This is explained by the fact that the phosphorus shallow donors will be fully ionized for the investigated range of temperatures. The deep energy levels $E_C - 0.17$ eV and $E_C - 0.107$ eV, which belong to VO_i and VO_iP complexes respectively [24], will be ionized only partially for the irradiated single crystals n−Si. The growth electron concentration with the increasing magnitude of the uniaxial pressure along the crystallographic direction [100] (Fig. 5, curves 2 and 5) can be explained with a decrease in the ionization energy of these complexes under the deformation [24], [25]. Only marginal increase in the electron concentration in the conduction band of silicon is observed at uniaxial pressures along the crystallographic direction [111] (Fig. 5, curves 3 and 4). In this case, the activation energy of the main radiation defects, belonging to the VO_iP complexes, decreases slightly and at P>0.4 GPa does not depend on the magnitude of uniaxial pressure [24].

3. THEORETICAL CALCULATIONS

To interpret the obtained temperature dependencies of Hall mobility of electrons for silicon samples, irradiated by the flux of electrons Ω=1·10^{17} el./cm^2 with the energy of 12 MeV at uniaxial pressures along crystallographic directions [100] and [111], we write the expression for the Hall mobility under condition of the scattering of electrons on the large-scale potential [28]:

$$\mu_H = \mu_0 A \exp\left(-\frac{\Delta}{kT}\right), \tag{1}$$

where μ_0 – drift mobility of electrons for homogeneous material, A – the Hall-factor, Δ – the amplitude of the large-scale potential.

$$\Delta = \frac{q^2 N^{2/3}}{\varepsilon \cdot n^{1/3}}, \tag{2}$$

where N – the concentration of charged defects, which is equal to the sum of concentrations of the ionized donors N_d and compensating charged acceptors N_a, ε – the dielectric penetration, n – the concentration of electrons in the conduction band, q – the charge of an electron.

Electron scattering on the ions of phosphorus impurity, acoustic phonons and optical phonons responsible for the intervalley scattering of electrons in silicon was taken into account at the calculations of the drift mobility of the electrons and the Hall factor. Mobility of charge carriers for any direction of isoenergetic surface, which is an ellipsoid of rotation, can be determined from the ratio [28]:

$$\mu = \mu_{\perp} \sin^2 \theta + \mu_{\parallel} \cos^2 \theta, \tag{3}$$

where θ – the angle between the considered direction and the main axis of ellipsoid; $\mu_{\perp}$ and $\mu_{\parallel}$ are the mobility of charge carriers across and along the axis of the ellipsoid, respectively.

In accordance with (3), for undeformed n-Si single crystals

$$\mu_0 = \frac{1}{3}\mu_{\parallel} + \frac{2}{3}\mu_{\perp}. \tag{4}$$

Under uniaxial pressure along the crystallographic direction [100], two minima of silicon conduction band will descend on the energy scale by a value [24]:

$$\Delta E_1 = -\left(\Xi_d + \frac{1}{3}\Xi_u\right)(S_{11} + 2S_{12})P - \frac{2}{3}\Xi_u (S_{11} - S_{12})P, \tag{5}$$

and the other four minima will ascend by a value:

$$\Delta E_2 = -\left(\Xi_d + \frac{1}{3}\Xi_u\right)(S_{11} + 2S_{12})P + \frac{1}{3}\Xi_u (S_{11} - S_{12})P. \tag{6}$$

If n_1 is the electron concentration in descending minima, and n_2 – in four minima which ascend at uniaxial pressure, then the total electron concentration in the conduction band of silicon is the following:

$$n = n_1 + n_2 . \tag{7}$$

For the non-degenerate electron gas:

$$n_1 = 2\left(\frac{2\pi m_1 kT}{\hbar^2}\right)^{3/2} e^{\frac{E_F - \Delta E_1}{kT}}, \; n_2 = 2\left(\frac{2\pi m_2 kT}{\hbar^2}\right)^{3/2} e^{\frac{E_F - \Delta E_2}{kT}}. \tag{8}$$

Then

$$\frac{n_2}{n_1} = \left(\frac{m_2}{m_1}\right)^{3/2} e^{\frac{\Delta E_1 - \Delta E_2}{kT}} = B, \tag{9}$$

where $m_1 = 2^{\frac{2}{3}}\left(m_{\parallel}\ m_{\perp}^2\right)^{\frac{1}{3}}$ and $m_2 = 4^{\frac{2}{3}}\left(m_{\parallel}\ m_{\perp}^2\right)^{\frac{1}{3}}$ are the effective mass of the density of states for these minima. Taking into account the value of the components of the effective mass tensor $m_{\parallel} = 0.9163m_0$ and $m_{\perp} = 0.1905m_0$ for electrons in silicon, $m_1 = 0.51m_0$ and $m_2 = 0.81m_0$were obtained.

From expressions (7) and (9), we find that

$$n_1 = \frac{n}{B+1}, n_2 = \frac{Bn}{B+1}. \tag{10}$$

According to (3), mobility of electrons in silicon at the uniaxial pressure along crystallographic direction [100] in the two descending minima is equal to:

$$\mu_1 = \mu_{\parallel}, \tag{11}$$

and for the four minima, which ascend on the energy scale,

$$\mu_2 = \mu_{\perp}. \tag{12}$$

Then for an arbitrary value of the uniaxial pressure P, the conductivity n−Si is the following:

$$\sigma_P = qn\mu = q\left(n_1\mu_1 + n_2\mu_2\right). \tag{13}$$

Taking into account expressions (10) and (13), electron mobility at the uniaxial pressure n−Si along the crystallographic direction [100] is equal to

$$\mu_0 = \frac{\mu_1 + B\mu_2}{B+1}. \tag{14}$$

The intervalley scattering of electrons on optical phonons is described by the scalar relaxation time [29]. As shown in research [26], intervalley scattering in the silicon is caused by the interaction of electrons with optical phonons at characteristic temperatures T_{C1}=190 K and T_{C2}=630 K. The constants of the optical deformation potential for these phonons $\Xi_{190} = 1.8 \cdot 10^8\ eV/cm$ and $\Xi_{630} = 4 \cdot 10^8\ eV/cm$ were found in the studies. The values of the constants of the acoustic deformation potential $\Xi_u = 9.23\ eV$ and $\Xi_d = 2.12\ eV$ are given in work [30]. Then, in the most general case of electron scattering on the impurity ions, acoustic phonons and optical phonons responsible for intervalley scattering, the expressions for the components of the relaxation time tensor can be written as follows [29]:

$$\frac{1}{\tau_{|}}=\frac{1}{\tau_{|}^{a,i}}+\frac{1}{\tau_1}+\frac{1}{\tau_2};\ \frac{1}{\tau_{\perp}}=\frac{1}{\tau_{\perp}^{a,i}}+\frac{1}{\tau_1}+\frac{1}{\tau_2}, \tag{15}$$

where $\tau_{|}^{a,i}$, $\tau_{\perp}^{a,i}$ are the longitudinal and transverse components of the relaxation time tensor for scattering on acoustic phonons and impurity ions, respectively; τ_1, τ_2 are the relaxation times for intervalley scattering on optical phonons at characteristic temperatures T_{C1}=190 K and T_{C2}=630 K.

In the case of uniaxial pressure along the crystallographic direction [111], an expression for the components of the effective mass tensor will be as follows [27]:

$$m_{11}=\frac{m_{\perp}}{1+\gamma P},\ m_{22}=\frac{m_{\perp}}{1-\gamma P},\ m_{33}=m_{\|}, \tag{16}$$

where $\gamma=6.74\cdot10^{-11}$ Pa^{-1}.

The deformation non-parabolicity of the conduction band of silicon, which explains the nonlinear growth of the tensoresistence and the dependence of tensoresistence on temperature for such uniaxial pressure, can be represented as follows [27]:

$$\varepsilon(P)=\varepsilon\left(1+\lambda\varepsilon\right)=\frac{\hbar^2}{2}\left(\frac{k_1^2}{m_{11}}+\frac{k_2^2}{m_{22}}+\frac{k_3^2}{m_{33}}\right), \tag{17}$$

where $\lambda=\lambda_0P^2$ is non-parabolicity parameters, $\lambda_0=20\ \frac{m^3}{N^3}$.

In this case, the mobility for uniaxialy deformed silicon is equal to:

$$\mu_0=\frac{1}{3}\left(\mu_{11}+\mu_{22}+\mu_{33}\right). \tag{18}$$

$$\mu_{11}=\frac{q}{m_{11}}<\tau_{11}>,\ \mu_{22}=\frac{q}{m_{22}}<\tau_{22}>,\ \mu_{33}=\frac{q}{m_{33}}<\tau_{33}>. \tag{19}$$

It is necessary to replace the variable $x=\frac{\varepsilon}{kT}$ with $x_1=x+\lambda kTx^2$ in the calculations of these mobility components.

Figures 3 and 4 (solid curves) present the theoretical calculations of the Hall mobility of electrons for irradiated n-Si single crystals, on the basis of expressions (14) and (18), under condition of electron scattering on phosphorus impurity ions, acoustic phonons and optical phonons responsible for intervalley scattering.

4. DISCUSSION OF THE OBTAINED RESULTS

From the analysis performed, it follows that for irradiated n-Si single crystals, Hall mobility with the increasing temperature initially increases and decreases during the crossing of the maximum. The growth of Hall mobility can be explained by two

reasons: 1) by decreasing of the amplitude of a large-scale potential with an increase of the electron concentration in the silicon conduction band due to the growth of temperature or deformation; 2) by decreasing of the concentration of charged defects belonging to the VO_iP and VO_i complexes, and, accordingly, the probability of scattering on such defects with the increasing temperature and uniaxial pressure. These reasons explain the growth of the magnitude of Hall electron mobility for the uniaxially deformed n-Si single crystals with an increase in the magnitude of uniaxial pressure to 0.42 GPa (Fig. 3, curve 3) and 0.37 GPa (Fig. 4, curve 3) at low temperatures. The decrease in the Hall mobility during the crossing of the maximum is due to the growing probability of intervalley scattering of electrons on the optical phonons with an increase in temperature. For such temperatures, the Hall mobility of electrons, as in the case of unirradiated silicon single crystals, decreases with an increase in the magnitude of uniaxial pressure. The slight difference between the obtained experimental results and the corresponding theoretical calculations is due to the fact that the relaxation time for electron scattering on the created radiation defects was not taken into account during the construction of the theoretical model of the Hall electron mobility for irradiated n-Si single crystals. Since radiation defects, as a rule, create deep energy levels in the band gap of a semiconductor and their microstructure is difficult to establish in many cases, it is a difficult task to simulate the potential of the interaction of an electron with such defects. Today, solving such problems is based on the creation of semi-empirical models of radiation defects, which often do not allow interpreting the obtained experimental results. However, the proposed theoretical model allows qualitatively and at certain temperatures quantitatively explaining the features of the temperature dependencies of the Hall mobility for the undeformed and uniaxially deformed n-Si single crystals with radiation defects.

5. CONCLUSIONS

The obtained experimental results and theoretical calculations show that for uniaxially deformed n-Si single crystals along crystallographic directions [100] and [111], irradiated by high-energy electrons, a decrease in a large-scale potential under the increase of temperature or magnitude of uniaxial pressure causes growth of the Hall mobility. Hall mobility of electrons for irradiated n-Si single crystals at the investigated temperatures and uniaxial pressures is determined by different relative contribution of the mechanisms of electron scattering on optical phonons, which are responsible for intervalley scattering, ions of phosphorus shallow impurities and large-scale potential. The results can be used for constructing, on the basis of n-Si single crystals of various electronic devices and sensors, strained silicon nanostructures (Si-quantum dots and quantum wells, heterostructures SiGe), which can be applied in the fields of high radiation and deformation. The presented theoretical model for calculating the Hall mobility of electrons for irradiated n-Si single crystals can be useful in modelling the electrical properties of other many-valley semiconductors with radiation defects, the presence of which leads to the emergence of large-scale potential.

REFERENCES

1. Yang, W., Chen, J., Zhang, Y., Zhang, Y., He, J. H., & Fang, X. (2019). Silicon-compatible Photodetectors: Trends to Monolithically Integrate Photosensors with Chip Technology. *Advanced Functional Materials, 29*(18), 1808182. DOI: 10.1002/adfm.201808182.
2. Goley, P. S., & Cressler, J. D. (2019). Silicon-Based Electronic Photonic Integrated Circuits: Resiliency in the Space Environment. *Georgia Institute of Technology Atlanta United States,* 220–223. Available at https://apps.dtic.mil/dtic/tr/fulltext/u2/1075341.pdf
3. Zhanshe, G., Fucheng, C., Boyu, L., Le, C., Chao, L., & Ke, S. (2015). Research Development of Silicon MEMS Gyroscopes: A Review. *Microsystem Technologies*, *21*(10), 2053–2066. DOI: 10.1007/s00542-015-2645-x.
4. Qin, Y., Howlader, M., & Deen, M. (2015). Low-temperature Bonding for Silicon-based Micro-optical Systems. *Photonics, 2*(4), 1164–1201. Multidisciplinary Digital Publishing Institute. DOI: 10.3390/photonics2041164.
5. Sharma, V., & Rajawat, A. (2018). Review of Approaches for Radiation Hardened Combinational Logic in CMOS Silicon Technology. *IETE Technical Review*, *35*(6), 562–573. DOI: 10.1080/02564602.2017.1343689
6. Nalwa, H. S. (ed.). (2001). *Silicon-based material and devices, two-volume set: materials and processing, properties and devices 1*. Academic Press.
7. Shimura, F. (ed.). (2012). *Semiconductor silicon crystal technology*. Elsevier Science & Technology.
8. Sun, Y., & Chmielewski, A. G. (eds.). (2017). *Applications of ionizing radiation in materials processing*. Institute of Nuclear Chemistry and Technology.
9. Gradoboev, A. V., & Simonova, A. V. (2017). Radiation Technologies in the Production of Semiconductor Devices. In *IX International Scientific and Practical Conference "Physical and Technical Problems in Science, Industry and Medicine",* 21–22 September 2017. Tomsk: TPU Publishing House.
10. Lee, B.J., Zhang, Z.M., Early, E.A., DeWitt, D.P., & Tsai, B.K. (2004). Modeling the Radiative Properties of Silicon with Thin-Film Coatings and the Experimental Validation. In *37th AIAA Therm Conf.,* 28 June–1 July 2004. Portland: OR.
11. Pagava, T. A., & Maisuradze, N. I. (2010). Anomalous Scattering of Electrons in n-Si Crystals Irradiated with Protons. *Semiconductors*, *44*(2), 151–154. DOI: 10.1134/S1063782610020041.
12. Gaidar, G. P. (2015). On the Tensoresistance of n-Ge and n-Si Crystals with Radiation-Induced Defects. *Semiconductors*, *49*(9), 1129–1133. DOI: 10.1134/S1063782615090110.
13. Funtikov, Y. V., Dubov, L. Y., Shtotsky, Y. V., & Stepanov, S. V. (2016). Radiation-Induced Defects in Si after High Dose Proton Irradiation. *Defect and Diffusion Forum, 373*, 209–212. Trans Tech Publications. DOI: 10.4028/www.scientific.net/DDF.373.209.
14. Yeritsyan, H. N., Sahakyan, A. A., Grigoryan, N. E., Harutyunyan, V. V., Grigoryan, B. A., Amatuni, G. A., & Rhodes, C. J. (2018). The Use of Different Pulsed Electron Irradiation for the Formation of Radiation Defects in Silicon Crystals. *Journal of Electronic Materials, 47*(7), 4010–4015. DOI: 10.1007/s11664-018-6286-6.
15. 15. Ciurea, M. L. (2013). Effect of Stress on Trapping Phenomena in Silicon: from Single Crystal to Nanostructures. *Romanian Reports in Physics*, *65*(3), 841–856.
16. Ding, L., Gerardin, S., Paccagnella, A., Gnani, E., Bagatin, M., Driussi, F., & Le Royer, C. (2015). Effects of Electrical Stress and Ionizing Radiation on Si-based TFETs. In *EUROSOI-ULIS 2015: 2015 Joint International EUROSOI Workshop and International Conference on Ultimate Integration on Silicon*, January 2015 (pp. 137–140). IEEE. Available at https://ieeexplore.ieee.org/document/7063792.

17. Momot, I., Malygina, H., Bertini, O., Heuser, J., Sturm, C., Teklishyn, M., & Lymanets, A. (2017). Studies of Radiation Field Impact on Microstrip Sensors for the CBM Silicon Tracking System. *Verhandlungen der Deutschen Physikalischen Gesellschaft*, *49*(44), 1.
18. Holbert, K. E., Nessel, J. A., McCready, S. S., Heger, A. S., & Harlow, T. H. (2003). Response of Piezoresistive MEMS Accelerometers and Pressure Transducers to High Gamma Dose. *IEEE Transactions on Nuclear Science, 50*(6), 1852–1859. Available at https://ieeexplore.ieee.org/document/1263811.
19. Marinaro, D. G., McMahon, P., & Wilson, A. (2008). Proton Radiation Effects on MEMS Silicon Strain Gauges. *IEEE Transactions on Nuclear Science, 55*(3), 1714–1718. Available at https://ieeexplore.ieee.org/document/4545162.
20. Vlasov, A.I., Mileshin, S., Tsivinskaya, T.A., & Shakhnov, V.A. (2018). Radiation Resistance of MEMS Sensors and Methods of Its Estimation. *Problems of Perspective Micro- and Nanoelectronic Systems Development, 4*, 190–196.
21. Sobolev, N. A. (2013). Radiation Effects in Si-Ge Quantum Size Structure. *Semiconductors*, *47*(2), 217–227. DOI: 10.1134/S1063782613020188.
22. Hao, M., Hu, H., Liao, C., & Wang, B. (2017). Effects of Gamma-Ray Radiation on Channel Current of the Uniaxial Strained Si Nano-scale NMOSFET. *IEICE Electronics Express, 14*(19), 20170866–20170866. DOI: 10.1587/elex.14.20170866.
23. Hao, M., Hu, H., Liao, C., Kang, H., Su, H., Zhang, Q., & Zhao, Y. (2017). Total Ionizing Dose Radiation Effect on the Threshold Voltage for the Uniaxial Strained Si Nano NMOSFET. *IEICE Electronics Express*, 14-20170411. DOI: 10.1587/elex.14.20170411.
24. Luniov, S., Zimych, A., Khvyshchun, M., Yevsiuk, M., & Maslyuk, V. (2018). Specific Features of Defect Formation in the nSi. *Eastern-European Journal of Enterprise Technologies*, *6*(12), 35–42. DOI: 10.15587/1729-4061.2018.150959.
25. Fedosov, A. V., Luniov, S. V., & Fedosov, S. A. (2011). Influence of Uniaxial Deformation on the Filling of the Level Associated with A-Center in n-Si Crystals. *Ukrainian Journal of Physics, 56*(1), 69–73. Available at http://archive.ujp.bitp.kiev.ua/files/journals/56/1/560108p.pdf.
26. Fedosov, A. V., Luniov, S. V., & Fedosov, S. A. (2010). Specific Features of Intervalley Scattering of Charge Carriers in n-Si at High Temperatures. *Semiconductors*, *44*(10), 1263–1265. DOI: 10.1134/S1063782610100039.
27. Baranskii, P. I., Kolomoets, V. V., & Korolyuk, S. S. (1983). The Non-parabolicity of the n-Si Conduction Band Caused by Elastic Deformation along the [111] Direction. *Physica Status Solidi (b)*, *116*(2), K109–K112. DOI: 10.1002/pssb.2221160241.
28. Luniov, S. V., Zimych, A. I., Nazarchuk, P. F., Maslyuk, V. T., & Megela, I. G. (2016). Specific Features of Electron Scattering in Uniaxially Deformed n-Ge Single Crystals in the Presence of Radiation Defects. *Radiation Effects and Defects in Solids*, *171*(11–12), 855–868. DOI: 10.1080/10420150.2016.1250094.
29. Luniov, S. V., Burban, O. V., & Nazarchuk, P. F. (2015). Electron Scattering in the Δ_1 Model of the Conduction Band of Germanium Single Crystals. *Semiconductors*, *49*(5), 574–578. DOI: 10.1134/S1063782615050140.
30. Luniov, S. V., Panasiuk, L. I., & Fedosov, S. A. (2012). Deformation Potential Constants Ξ_u and Ξ_d in n-Si Determined with the Use of the Tensoresistance Effect. *Ukrainian Journal of Physics*, *57*(6), 636–641. Available at http://archive.ujp.bitp.kiev.ua/files/journals/57/6/570608p.pdf

ELEKTRONU IZKLIEDĒJUMA MEHĀNISMI VIENASS DEFORMĒTOS ATSEVIŠĶOS SILIKONA KRISTĀLOS AR RADIĀCIJAS DEFEKTIEM

S.V. Luniovs, V.V. Lišuks, V.T. Masļuks, O.V. Burbans

K o p s a v i l k u m s

Aprakstīti elektronu Holla mobilitātes temperatūras atkarības mērījumi vienass deformētiem atsevišķiem n-Si kristāliem, ko izstaro elektronu plūsma $\Omega=1\cdot10^{17}$ el./cm^2 ar enerģiju 12 MeV iegūti, balstoties uz piezo-Holla efekta mērījumiem. No šo mērījumu analīzes izriet, ka pie vienass spiediena (0–0.42) GPa un (0–0.37) GPa kristalogrāfiskajos virzienos ir novērojams deformāciju ierosināts Holla mobilitātes pieaugums. Balstoties uz piedāvāto mobilitātes teorētisko modeli, šis pieaugums ir izskaidrojams ar liela mēroga potenciāla amplitūdas samazināšanos, vienass deformāciju magnitūdas palielināšanos un attiecīgi iespējamu elektronu izkliedējumu.

20.09.2019.